1   **Catastrophic failure: how and when? Insights from 4D in-situ x-ray micro-**
2   **tomography**

3   **Alexis Cartwright-Taylor[1], Ian G. Main[1], Ian B. Butler[1], Florian Fusseis[1], Michael Flynn[1]**
4   **and Andrew King[2]**

5   [1]School of Geosciences, University of Edinburgh, James Hutton Road, Edinburgh EH9 3FE, UK.
6   [2]SOLEIL Synchrotron, L'Orme des Merisiers Saint Aubin, Gif-sur-Yvette, France.

7   Corresponding author: Alexis Cartwright-Taylor alexis.cartwright-taylor@ed.ac.uk

8   **Key Points:**

9   • Micron-scale crack network evolution and localization is imaged *in-situ* in deforming
10 granite samples with controlled initial heterogeneity

11 • Heterogeneity affects order and predictability of the phase transition to failure, which
12 occurs as correlation length approaches grain size

13 • Correlation dimension of the crack population is a key indicator of localization, and
14 anisotropy in starting porosity dictates fault strike
15

16 **Abstract**

17 Catastrophic failure of brittle rocks is important in managing risk associated with system-sized
18 material failure. Such failure is caused by nucleation, growth and coalescence of micro-cracks that
19 spontaneously self-organize along localized damage zones under compressive stress. Here we
20 present x-ray micro-tomography observations that elucidate the *in-situ* micron-scale processes,
21 obtained from novel tri-axial compression experiments conducted in a synchrotron. We examine
22 the effect of microstructural heterogeneity in the starting material (Ailsa Craig micro-granite;
23 known for being virtually crack-free) on crack network evolution and localization. To control for
24 heterogeneity, we introduced a random nano-scale crack network into one sample by thermal
25 stressing, leaving a second sample as-received. By assessing the time-dependent statistics of crack
26 size and spatial distribution, we test the hypothesis that the degree of starting heterogeneity
27 influences the order and predictability of the phase transition between intact and failed states. We
28 show that this is indeed the case at the system scale. The initially more heterogeneous (heat-treated)
29 sample showed clear evidence for a second-order transition: inverse power-law acceleration in
30 correlation length with a well-defined singularity near failure, and distinct changes in the scaling
31 exponents. The more homogeneous (untreated) sample showed evidence for a first-order
32 transition: exponential increase in correlation length associated with distributed damage and
33 unstable crack nucleation ahead of abrupt failure. In both cases, anisotropy in the initial porosity
34 dictated the fault orientation, and system-sized failure occurred when the correlation length
35 approached the grain size. These results have significant implications for the predictability of
36 catastrophic failure in different materials.

37 **Plain Language Summary**

38 When rocks deform, tiny cracks appear, increasing in size and number until the rock breaks
39 completely, often along a narrow plane of weakness where cracks have spontaneously aligned.
40 Sometimes, when the microstructure is complicated, cracking accelerates quickly in a predictable
41 way, giving a good indication of when the rock will break. In other cases, when the microstructure
42 is more uniform, cracking accelerates more slowly and the rock breaks suddenly and early. To
43 understand why failure is predictable in some cases but not others – a major problem in managing
44 risk from material failure (e.g., earthquakes) – we used x-ray imaging to see how cracks form and
45 interact with each other inside deforming rocks. We found that predictable behavior only arose
46 when cracks aligned themselves asymmetrically. The orientation of this damage zone was
47 governed by the rock's pre-existing microstructure. We also found distinct changes in crack size
48 and spatial arrangement during alignment, indicating that the rock was approaching failure.
49 However, when cracks did not align asymmetrically, similar changes were not observed and failure
50 was not predictable. Our results are important because they help explain why reliable indicators of
51 catastrophic failure are not always observed and why forecasting may only work in certain cases.
52

53 **List of Symbols (in order of appearance)**

variable	symbol
correlation length (typical linear dimension of largest void)	ξ
time	t
critical (failure) time	t_c
axial sample strain	ϵ
critical (failure) strain	ϵ_c
strain rate	$\dot{\epsilon}$
differential stress	σ
axial stress	σ_1
confining pressure (radially-symmetric)	σ_3
sample length	L
critical (failure) stress	σ_c
sample co-ordinate system	x, y, z
dip	ϕ
strike	θ
porosity	φ
number of segmented voids	N
individual void	i
volume of an individual void (pore or micro-crack)	V_i
volume of the largest void	V_{max}
sample radius	R
length of analyzed sub-volume	l
volume of analyzed sub-volume	V_{subvol}
corrected Akaike Information Criterion	$AICc$
first-order moment of inertia (void centroid)	M
second-order moment of inertia (covariance matrix)	I
void ellipsoid radius	r
mean void ellipsoid radius	$\bar{r}$
power-law exponent of void volume distribution	β
Euclidean distance between two voids (inter-void distance)	L_i
two-point correlation (fractal) dimension (power-law exponent of inter-void distance distribution)	D
cumulative complementary (survivor) function of frequency-volume distribution	$\Phi(V)$
completeness threshold of frequency-volume distribution	V_t
tapering corner threshold of frequency-volume distribution	V_c
modified Bayesian Information Criterion	BIC
incremental probability distribution of inter-void lengths	$P(L_i)$
exponent of incremental inter-void length distribution	D_{inc}

54

1 Introduction

Catastrophic failure of rocks in the brittle Earth is a critically-important driving mechanism for phenomena such as landslides, volcanic eruptions and earthquakes, including induced seismicity. Such failure often happens suddenly and with devastating consequences, occurring when structural damage, in the form of smaller faults and fractures, concentrates within localized zones. Damage localization leads to weakening and stress redistribution, eventually resulting in system-sized brittle failure along a distinct and emergent fault plane. Localized damage is pervasive at all scales throughout the brittle crust (Mitchell and Faulkner, 2012) and is therefore a fundamental control on catastrophic failure. Crack nucleation and growth, and crack coalescence within already localized zones, are relatively well-understood from microstructural and field observations of damaged rocks, and from monitoring and locating earthquakes and acoustic emissions (elastic wave packets released during laboratory-scale micro-fracturing events). However, the process of localization remains elusive. Smaller cracks spontaneously self-organize along the incipient fault plane, often immediately before failure, but the precise mechanisms involved in this self-organization have yet to be determined. Open questions include: (i) how do cracks, pores and grain boundaries interact locally with the applied stress field to cause catastrophic failure to occur at a specific place, orientation and time? (ii) why can we detect precursors to catastrophic failure only in some cases?

Fractures and faults have a self-similar structure; they are scale-invariant in their length and spatial distributions (Main et al., 1990; Main, 1996; Bonnet et al., 2001), and in the way their size relates to the energy released during rupture (Abercrombie, 1995; Goodfellow and Young, 2014). Remarkably, earthquakes and acoustic emissions (AE) are indistinguishable apart from the absolute source size, with scaling characteristics that are invariant over 15 orders of magnitude (Goodfellow and Young, 2014). This behavior is controlled by the local stress state and rock mass properties. Classically, brittle rock deformation and failure have been characterized by AE, with progressive cracking in heterogeneous materials under stress leading to systematic changes in the AE event rate and its frequency-magnitude distribution. Experiments have shown that pervasive microcracking accumulates in the sample sub-critically, i.e., without causing system-sized failure (Lockner et al., 1991; Lei et al., 2000), until the accumulating cracks self-organize along an asymmetric, localized damage zone. System-scale failure then occurs when nucleating micro-cracks have localized sufficiently for a runaway positive feedback of self-sustaining crack propagation and coalescence to take over (Main et al., 1993). In some cases, this self-organization becomes evident in the emergence of an inverse power-law acceleration of event rate with a well-defined failure time. In others, system-sized failure of rock samples is commonly associated with the transition from an exponential increase to a sudden, rapid acceleration in the AE event rate close to peak stress (Sammonds et al., 1992; Moura et al., 2005; Vasseur et al., 2015). This transition occurs exactly when cracks begin to localize along the incipient fault plane (Lockner et al., 1991). At this crucial point, nucleated cracks grow by jumping geometrical and rheological barriers, so regions of stress concentration must already be correlated at the scale of the incipient fault network (Sammis and Sornette, 2002). The organized fracture network then propagates dynamically, with macroscopic failure occurring at a well-defined, finite time as the power-law reaches its asymptote.

This behavior indicates a transition from pervasive but stable crack growth, controlled by the sample's microstructure, to an unstable regime of dynamic rupture along an organized fracture network, controlled by stress and fracture mechanics (Guéguen and Schubnel, 2003; Alava et al.,

4

100 2008). The inverse power law transition can be described as a critical or second-order phase
101 transition; a continuous transition from one state to another, during which the system becomes
102 extremely susceptible to external factors. It is second-order if the first derivative of the free energy
103 of the system (an entropy term) changes continuously as a function of the control parameter, e.g.,
104 temperature (Stanley, 1971, Fig. 2.6) or, in the case of a constant strain (or stress) rate rock
105 deformation experiment, strain (or stress). This is associated with an inverse power law
106 acceleration of the correlation length towards the critical point (Bruce and Wallace, 1989). At this
107 point, strong correlations exist between all parts of the system (including at long-range) and many
108 length scales become relevant (resulting in a self-similar structure and power-law scaling), with
109 events occurring at all relevant length scales (associated with broadband self-similarity of
110 correlations). The transition to an inverse power-law in the AE event rate, with its 'finite-time
111 singularity' at failure, is also characteristic of a second-order or critical phase transition (Sammis
112 and Sornette, 2002). If this occurs in the lead up to macroscopic failure, then the failure time can
113 be forecast accurately (Vasseur et al., 2015; 2017). Inverse power-law acceleration to a well-
114 defined failure time has also been seen in the evolving microstructure (micro-crack porosity and
115 the volume of the largest micro-fracture) of crystalline rocks undergoing brittle deformation
116 (Renard et al., 2017; 2018).

117 However, the evolution of damage does not always allow a fit to a model with a well-
118 defined failure time. In structurally homogeneous materials, there is no emergent, smooth power-
119 law acceleration to failure, as shown experimentally by Vasseur et al. (2015; 2017) for a range of
120 rock types and material analogues. In the extreme case of a single flaw in an otherwise uniform
121 starting material, there is no precursor, and catastrophic system-sized failure occurs suddenly when
122 the flaw propagates dynamically at a maximum in the system free energy. In turn, this depends on
123 the applied stress, the length of the starting flaw, and the specific surface energy of the material
124 (Griffith, 1921; 1924). This results in a discontinuous or first-order transition between intact and
125 failed states. In real materials that possess only a small amount of microstructural disorder,
126 progressive subcritical cracking, i.e., cracking which does not fulfil the conditions for sustained
127 propagation, shows only an exponential increase in the event rate time-to-failure behavior (Vasseur
128 et al., 2015; 2017). Failure occurs suddenly and early; often much earlier than expected from an
129 exponential asymptote (Vasseur et al., 2015; 2017). This behavior is also characteristic of an abrupt
130 first-order transition, with the exponential behavior reflecting local correlations (Stanley, 1971;
131 Sethna, 2006).

132 Phase transitions are often characterized by the evolution of the correlation length and
133 scaling exponents of the system in question (Stanley, 1971). The correlation length, ξ, is the
134 distance over which the effects of a local perturbation of the system will spread (Thouless, 1989).
135 Close to a critical point, the system can be viewed as made up of regions of size ξ in the critical
136 state. In this case, ξ can be interpreted as the size of the regions of the nucleating phase, or the
137 typical linear dimension of the largest piece of correlated spatial structure (Bruce and Wallace,
138 1989), which in our case is approximately the length of the largest fracture. As the two phases
139 (intact and failed) compete to select the final equilibrium state, regions closer than ξ are correlated
140 and those further apart are uncorrelated. Approaching the critical point, the correlated (nucleating)
141 regions become comparable to the system size. Thus, the maximum correlation length, and
142 associated parameters such as the maximum AE magnitude, are restricted by the system size.

143 During a first-order transition, the correlation length ξ becomes macroscopically large but
144 remains finite until the discontinuity at the sudden change of state (Stanley, 1971). In the case of

a single Griffith crack, the correlation length is simply the length of the starting flaw, which suddenly becomes system-sized at failure as the flaw propagates instantaneously through the material (Figure 1, blue line). When real, structurally homogeneous materials, with a dilute population of material flaws, undergo progressive subcritical cracking (e.g., Vasseur et al., 2015; 2017), we expect the correlation length to increase exponentially but remain finite until it becomes system-sized at a sudden-onset discontinuity (Figure 1, orange line). Conversely, during a continuous phase transition, the correlation length ξ becomes effectively infinite (Figure 1, green line), growing as an inverse power-law function of the control parameter (e.g., temperature), T, approaching the critical point, T_c (Bruce and Wallace, 1989):
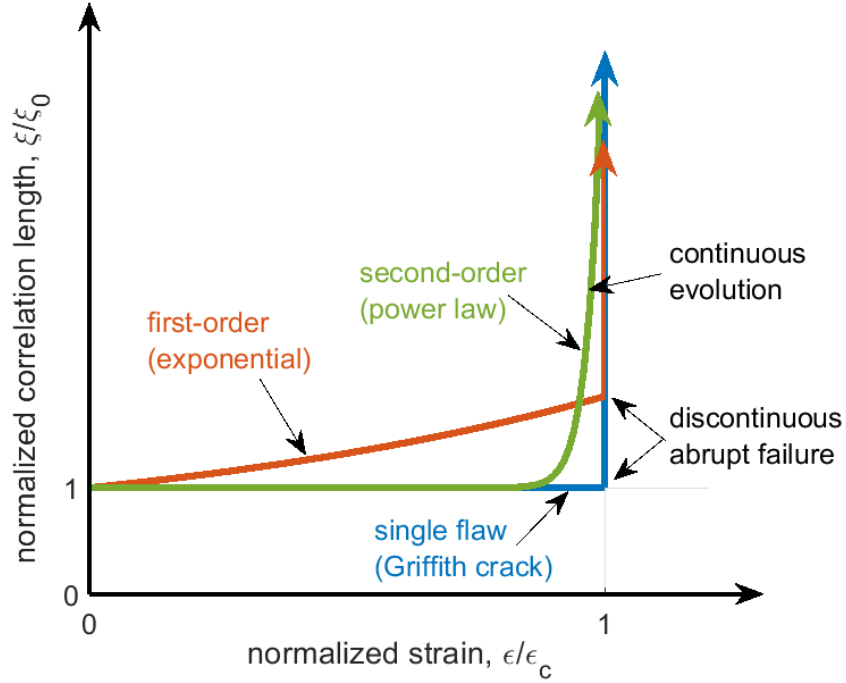
$$\xi \sim (T_c - T)^{-\nu} \tag{1}$$

This is the type of behavior is associated with progressively more heterogeneous materials undergoing brittle deformation (Vasseur et al., 2015; 2017). In summary, the degree of microstructural disorder of a material exerts a strong control on the type of phase transition from subcritical crack growth to dynamic rupture, and consequently the predictability of the transition. In particular, experiments (Vasseur et al., 2017) and models (Kun et al., 2018) have shown that heterogeneity strongly influences the spatial distribution of micro-cracks at failure.

Here we investigate the impact of material heterogeneity on the nature of the phase transition between intact and failed states, and the associated predictability of failure, at the micron-scale. We show how the micro-crack network evolves within a deforming crystalline rock with different amounts of disorder. Since pre-existing cracks are the most dominant factor of all heterogeneities that govern the fault nucleation process in laboratory rock samples (Lei et al., 2000), we deformed two samples of Ailsa Craig micro-granite: one being an as-received control (nominally crack-free), and the other containing a pre-existing nano-scale crack network, induced by thermal stress, as a proxy for increased heterogeneity. Ailsa Craig samples, as received from the quarry, have no detectable cracks on thin sections under both optical and scanning electron microscopes (Meredith et al., 2005; 2012). They are an extreme end member of lowest crack density in natural rocks. Through the analysis of 4D, *in-situ* synchrotron x-ray micro-tomography (μCT) images of the two samples undergoing tri-axial deformation (see Cartwright-Taylor et al. (2020) for access to the dataset), we test the hypothesis that the transition to failure is abrupt and unpredictable (first-order) in the as-received sample (our initially crack-free end member), but is continuous and predictable (second-order) in the pre-cracked sample. *In-situ* observation of the deforming microstructure allows us to measure directly the relevant parameters such as the correlation length and the scaling exponents.

We find that increasing the microstructural disorder affects the geometry, size and spatial distribution of the evolving micro-fractures. Using a combination of visual inspection of the μCT images, geometrical analysis of the evolving crack network, and techniques used in statistical seismology, we show that the micro-crack network evolution varies significantly between the two samples. The degree of starting heterogeneity controls (i) the evolving spatial clustering and anisotropy of the micro-cracks, and (ii) the order of the phase transition. The initially crack-free sample exhibits an exponential increase in damage that reflects local correlations, a finite correlation length, and no obvious precursors to failure. In contrast, the pre-cracked sample exhibits emergent power-law behavior, an inverse power-law acceleration to infinite correlation length and clear precursors to failure. However, though the parameters may be different, the power-law scaling of the micro-crack volume and inter-crack length distributions, and some crack growth characteristics, appear independent of heterogeneity. Allowing for the fact that such

189 microscopic failure characteristics may not be detectable above ambient noise in a field
190 experiment, this may explain why measureable geophysical precursors to catastrophic failure
191 events are detected only in some cases.

192

193   **Figure 1:** Schematic graph showing the expected behavior of the correlation length ξ,
194 normalized by its initial value ξ_0, as strain ϵ increases towards failure at critical strain ϵ_c for the
195 three phase transition cases described in the text. The Griffith crack (blue line) and the exponential
196 (orange line) are both examples of first-order transitions, exhibiting abrupt failure evident as the
197 discontinuity in ξ at ϵ_c. The inverse power-law (green line) shows the smooth, continuous
198 evolution to failure characteristic of a second-order transition.

199 **2   Materials and Methods**

200   **2.1   Ailsa Craig micro-granite and thermal stressing**

201   We used Ailsa Craig micro-granite (ACM) from the island of Ailsa Craig in the Firth of
202 Clyde, Scotland. ACM is an extremely rare type of silica-unsaturated, alkali-rich microgranite,
203 known as Blue Hone (Meredith et al., 2012). As received from the quarry, no pre-existing
204 microcracks are detectable either by optical or scanning electron microscopy (Meredith et al.,
205 2005; 2012). Porphyritic in texture with a groundmass of mean grain size 250 μm, ACM contains
206 sparsely distributed microphenocrysts (up to 1.5 mm) of alkali feldspar (Odling et al., 2007). Clint
207 et al. (2001) found it to have extremely low porosity (<< 1 %) and permeability (1.5 x 10^{-23} m^2 at
208 10 MPa effective pressure), indicating that the small amount of pre-existing pores are
209 predominantly unconnected (e.g., see Fig. 3 top left in Meredith et al., 2012). These properties
210 make ACM ideal both for its main commercial use as the running surface of curling stones, and
211 for the purposes of this study. We chose ACM for two main reasons: (i) its small grain size (250
212 μm) and (ii) its virtually crack-free nature. The former is essential to ensure a statistically
213 significant number of grains (>10 grains per diameter) in the small (3 mm diameter x 9 mm long)
214 cylindrical samples, and so to ensure that such small samples are representative of the rock as a
215 whole. The latter is essential to allow comparison between two extreme end-members: (i) an as-
216 received control sample with the lowest possible (to our knowledge) pre-existing crack density,
217 and (ii) a second sample (from the same small block) containing a thermally-induced crack
218 network imprinted over the nominally crack-free microstructure, thus increasing its heterogeneity
219 compared with the initially crack-free (untreated) sample.

220   To introduce a network of micro-cracks, one sample was heated slowly to 600 °C prior to
221 deformation. Thermal stressing is one of the key fracture-generating mechanisms in crustal rocks
222 and is an effective method for introducing micro-fractures into rock samples. Heating ACM to
223 elevated temperatures (>500 °C) induces significant, permanent micro-crack damage, evident from
224 photomicrographs (Meredith et al., 2012) and up to 50% and 30% reduction in P- and S- wave
225 velocities respectively (Clint et al., 2001). Scanning electron micrograph observations (Odling et
226 al., 2007) show that heating ACM to 900 °C causes the formation of a permanent micro-crack
227 network with average aperture of 0.3 μm formed by tensile failure, with each crack nucleating
228 halfway along a previous one to generate fracture intersections of primarily T-shaped geometry.
229 The thermally-induced crack network is not discernible in our μCT data because this aperture is
230 less than one tenth the length of one pixel (2.7 μm). Due to the partial volume effect, micro-cracks
231 with an aperture smaller than half a pixel are not visible (e.g., Voorn et al., 2013).

232   **2.2   Experimental apparatus, sample assembly and loading protocol**

233   Synchrotron x-ray microtomography (μCT), in combination with x-ray transparent
234 pressure vessels (e.g., Fusseis et al., 2014; Renard et al., 2016; Butler et al., 2017), allow the
235 microstructural evolution of deforming rock samples to be imaged directly, non-invasively and *in-*
236 *situ* during an experiment. This provides a critical advantage over conventional deformation
237 experiments, where the evolution of microscopic deformation cannot be inferred from post-test
238 analysis of the microstructure because it is heavily overprinted by extensive damage caused during
239 the macroscopic rupture process. Even in the case where conventional experiments are stopped
240 immediately prior to macroscopic failure, overprinting occurs when the hydrostatic and differential
241 stresses are released during extraction of the sample from the steel-walled pressure vessel,
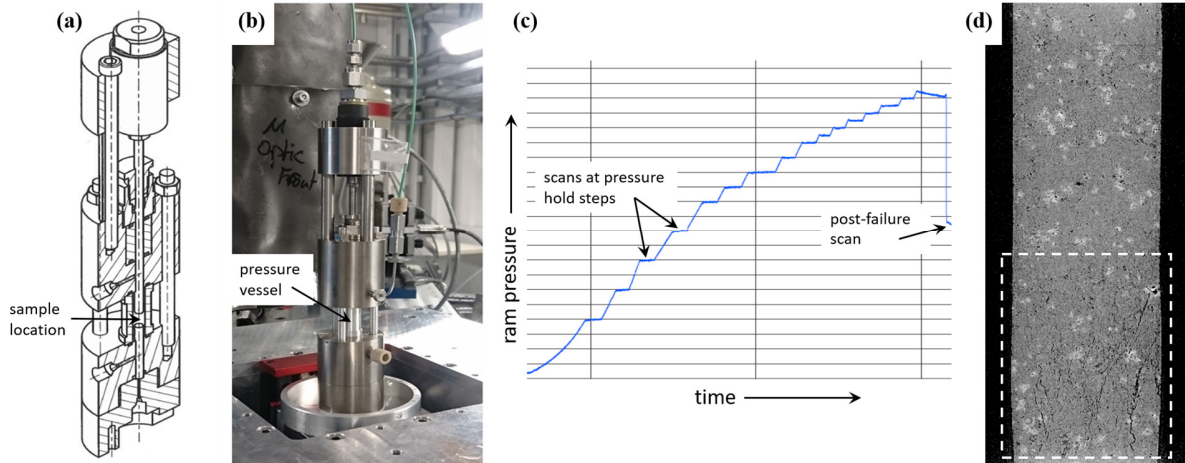
242 resulting in permanent damage and hysteresis. *In-situ* x-ray μCT imaging overcomes both these
243 issues, as well as providing detailed microstructural information about the temporal evolution of
244 damage accumulation at a much higher temporal resolution. A single time-resolved experiment is
245 equivalent to tens of conventional experiments with *ex-situ*, post-experiment analysis, and has the
246 virtue that the same sample is observed at each time-step rather than a suite of samples, removing
247 the issue of sample variability.

248 In our experiments, each sample of ACM underwent tri-axial deformation to failure. The
249 experiments were conducted using a novel, miniature, lightweight (<1.3 kg) x-ray transparent tri-
250 axial deformation apparatus Mjölnir', developed and tested at the University of Edinburgh.
251 Mjölnir, named for the hammer of Thor, the Norse god of thunder, accommodates samples of 3
252 mm diameter and up to 10 mm in length and is designed to operate up to confining pressures of 50
253 MPa and axial stress in excess of 622 MPa (Butler et al., 2017). For this study, Mjölnir was
254 installed on the μCT rotation stage at the PSICHE beamline at SOLEIL Synchrotron, Gif-sur-
255 Yvette, France (Figure 2a,b). Two cylindrical samples of ACM, one heat-treated and one untreated
256 were cored using a diamond core drill and the ends ground flat and parallel to achieve 3 mm outside
257 diameter and 9 mm length, compared to the typical grain size of 250 μm. Even though this sample
258 diameter is very small (required to obtain high-resolution μCT images), the small grain size means
259 that there are more than 10 grains per diameter, ensuring that such small samples are representative
260 of the rock as a whole. The sample was assembled between the two pistons, jacketed with silicone
261 tubing (3.18 mm internal diameter and 0.79 mm wall thickness), and protected from the confining
262 fluid using twisted wire loops to seal the jacket against the piston (Butler et al., 2017). The pressure
263 vessel was lowered over the sample assembly and fixed into place. A confining pressure of 15
264 MPa was then applied and maintained during the test. A hydrostatic starting pressure condition
265 was achieved by simultaneously increasing the axial pressure to match the confining pressure.
266 Delivery of the pressurizing fluid, deionized water, to the hydraulic actuator and pressure vessel
267 was achieved using two Cetoni neMESYS^{TM} high pressure syringe pumps operated with
268 QmixElements^{TM} software.

269 Experiments were conducted at room temperature under nominally dry conditions. A
270 reference μCT scan was acquired at zero differential stress to obtain the initial state of the sample
271 prior to loading. The sample was then loaded to failure at a constant strain rate of 3 x 10^{-5} s^{-1} in a
272 step-wise manner, with steps of 20 MPa to start with, decreasing to 10 MPa from 70% of the failure
273 strength and then 5 MPa once the sample started to yield (Figure 2c). At each step the stress was
274 maintained and a μCT volume acquired. To accommodate the full sample length at maximum
275 resolution, three sequential scans were acquired at different positions along the length of the
276 sample and then stacked. For each position the corresponding projections that comprised the full
277 length of the sample were tessellated and merged to create a single projection used for
278 reconstruction of the whole sample in one μCT volume. Each full set of scans was acquired in
279 approx. 10 minutes. For each sample, 15 sets were acquired during loading with an additional set
280 acquired after the main failure. For the heat-treated sample, this included one set at peak
281 differential stress of 185 MPa. This μCT volume contained the incipient fault at the critical point
282 of failure, and the sample failed immediately upon continuation of the loading procedure. The
283 untreated sample reached a peak stress of 182 MPa but failed before it could be scanned at this
284 stress. The last pre-failure scan was at 177 MPa (97% of the critical failure stress, σ_c).

285 The differential stress is $\sigma = \sigma_1 - \sigma_3$, where σ_1 is the axial stress (the product of the
286 measured ram pressure and the difference in area between the ram and the sample cross-section)

287 and σ_3 is the radially-symmetric confining pressure. Axial sample strain was calculated as $\epsilon =$
288 $\delta L/L_0$, where δL is the change in length of the sample between the starting µCT volume and the
289 volume of interest and L_0 is the initial length of the sample. It was obtained directly from the
290 reconstructed µCT volumes by measuring the length change of the rock core between two fixed
291 locations in each volume.

292

293 **Figure 2:** Our x-ray transparent deformation apparatus, Mjölnir, in (**a**) schematic (Butler
294 et al., 2017), and (**b**) installed at the PSICHE beamline. (**c**) Stepped loading procedure. (**d**)
295 Reconstructed µCT image showing damage accumulation at one end of the sample (this occurred
296 in both samples) – dashed white line shows the analyzed sub-volume.

2.3 X-ray imaging and image data pre-processing

298 X-ray µCT data was acquired using an sCMOS (scientific Complementary-Metal-Oxide
299 Semiconductor) Hamamatsu ORCA Flash4.0 camera, with a Rodagon 50 lens, giving about 2.5x
300 magnification (effective pixel size 2.7 µm), and a 250 µm thick LuAG:Ce scintillator. The white
301 beam with an average detected energy of about 66 keV was filtered with 1 mm aluminium and 0.5
302 mm tungsten. During each scan, 1200 projections were acquired over 180°, with an exposure time
303 per projection of 15-19 ms depending on the progressive darkening of the objective lens. A mix of
304 absorption and phase contrast data was acquired, with a sample to detector distance of 125 mm.

305 Each µCT volume was reconstructed by filtered back projection. Reconstructions were
306 performed at the PSICHE beamline, using both x-ray absorption and phase contrast modes as
307 implemented in the PyHST2 software (Mirone et al., 2014), and yielded 3D volumes of 1700 x
308 1700 x 4102 equidimensional voxels, with a voxel edge length of 2.7 µm. These volumes were
309 then processed to extract the fracture network from the reconstructed images. To deal efficiently
310 with the huge size of each 3D volume (approx. 40 GB) and speed up the subsequent processing,
311 we selected a sub-volume of interest – the region in the failed samples where the majority of
312 damage had accumulated (Figure 2d, Table 1). Using the Avizo™ software package, this sub-
313 volume was extracted from each of the full 3D volumes and de-noised with an anisotropic diffusion
314 filter (stop value 0.4 over 4 iterations), which was chosen to emphasize the microcrack features as
315 it preserves strong edges and enhances edge contrast. It was then down-sampled to 16-bit with a
316 32-bit threshold range of -0.3 to 0.8, yielding individual datasets of manageable size (approx. 3
317 GB).

318 **Table 1:** Dimensions of the whole sample and analyzed sub-volume, with uncertainties to
319 two decimal places.

sample	sample diameter (mm)	sample length (mm)	ROI length (mm)	ROI area (mm²)	ROI volume (mm³)
untreated [ACfresh02]	2.96	8.73	3.33	6.62	22.03
heat-treated [ACHT01]	2.97	9.46	2.71	6.58	17.83

320 ## 2.4   Segmentation

321 Each dataset of 3D grey-scale images was then segmented to separate from the rest of the
322 rock matrix the pre-existing pores and the evolving deformation-induced cracks in a binary
323 fashion. Herein we use the term 'porosity' to include all the segmented void space in the sample,
324 whether pre-existing (and therefore associated with the igneous history of the rock) or
325 deformation-induced. We use the term 'void' to describe an individual segmented object.

326 Although easily distinguishable by the human eye, narrow planar features such as fractures
327 are difficult to extract automatically from large 3D image datasets. This is due to the range of
328 greyscale values accommodated by fractures of different apertures and the increasing similarity of
329 these grey-values to the surrounding rock matrix as the aperture decreases. The main reason for
330 this is the partial volume effect, whereby voxels containing both air and rock matrix appear brighter
331 than voxels containing air alone. Fracture surface roughness and narrow apertures contribute to
332 this effect. We used a multiscale Hessian fracture filter (MSHFF) technique to meet these
333 challenges while still using an automated approach and segment the micro-cracks from the image
334 data. This technique, developed and described in detail by Voorn et al. (2013), uses the Hessian
335 matrix (second-order partial derivative of the input image data) to represent the local curvature of
336 intensity variation around each voxel in a 3D volume (e.g., Descoteaux et al., 2005). Attributes of
337 this local curvature can be used to distinguish planar features in the dataset (Text S1a in our
338 Supporting Information, SI). The analysis is conducted over a range of observed crack apertures,
339 which are combined to produce the final multiscale output: narrow fractures of varying apertures
340 detected within the 3D image data. The analysis was carried out using the macros for FIJI
341 (Schindelin et al., 2012) published by Voorn et al. (2013), utilizing the FeatureJ plugin (Meijering,
342 2010) to calculate the Hessian matrices, with input parameters given in (Table 2).
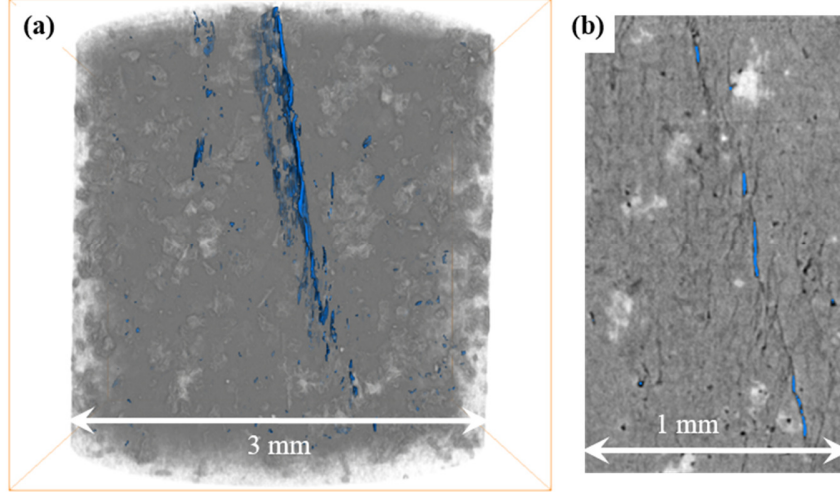
343 **Table 2:** Input parameters for segmentation code. Definitions given in Voorn et al. (2013).

smin	smax	sstep	blocksize	avgmat	consthresh	maxmat	padding	mincal	maxcal
2	8	1	1037	65535	0	56540	0	0.14118	0.32549

344 The binary segmented volumes were labelled and an intensity radius threshold of 15 to 100
345 applied followed by a small spot filter to remove round segmented objects with a radius of <50
346 pixels (134 μm) for visual clarity of the fault plane (Figure 3a). The local aperture at each voxel
347 of the segmented voids was computed from the diameter of the largest ball containing the voxel
348 and entirely inscribed within the object (Hildebrand and Ruegsegger, 1997). Even with the
349 segmentation method described, there is still significant under-sampling of the void population,
350 particularly at the narrower end of the aperture range (Figure 3b). Further work in this area is
351 required and would benefit from machine learning approaches (Andrew, 2018).

352 We present the data according to a co-ordinate system (x, y, z) where z is the vertical axis,
353 which is parallel to the loading direction and corresponds to the direction of axial stress (σ_1). The
354 other two (x and y) are the horizontal axes, which are perpendicular to the loading direction and

355 correspond to the confining stress ($\sigma_2 = \sigma_3$) with their directions arbitrarily assigned but consistent
356 between the two experiments. Void orientations are given in terms of their dip ϕ (deviation from
357 horizontal) and strike θ (deviation from y).

358

359 **Figure 3:** (**a**) Segmented fracture network (blue) within a greyscale 3D μCT sub-volume
360 at peak stress in the heat-treated sample. (**b**) Example of a 2D grey-scale slice, also with segmented
361 fractures highlighted in blue. Most of the very narrow fractures remain undetected due to the
362 similarity of the grey-scale values with the surrounding material.

363 **2.5   Analysis of the segmented microcrack network**

364 *2.5.1   Porosity and the number of fractures*

365 Initially of interest is the evolution of porosity, φ (including both the pre-existing pores
366 and the developing micro-cracks) and the total number of voids, N, in each 3D sub-volume as
367 deformation progressed. Due to the irregular shape of the segmented objects, and to take into
368 account crack coalescence, one void was defined as all objects that were connected at least by the
369 apex of a corner. To obtain N, each individual void, i, was assigned a label using the Label
370 Analysis module in Avizo™. Porosity was obtained from the total void volume divided by the
371 analyzed sub-volume: $\varphi = (\sum V_i)/(\pi R^2 l)$, where V_i is volume of each crack, R is the sample
372 radius and l is the length of the analyzed sub-volume. To determine the most likely empirical
373 relationship with strain for both φ and N, we found the parameters for several possible models
374 (quadratic, exponential and simple power-law) using non-linear least-squares regression and then
375 used the corrected Akaike Information Criterion, $AICc$ (Hurvich and Tsai, 1989) to test these
376 competing models objectively (see Text S2 in the SI for a full description of the calculations).

377 *2.5.2   3D micro-crack orientations and geometries*

378 These were obtained from the binary segmented data using an object-based approach to
379 determine the best-fitting ellipsoid around each segmented void (pore or micro-crack). Each
380 ellipsoid was calculated independently from the crack's 3D moments of inertia (Text S1b in SI),
381 also using the Label Analysis module in Avizo™. First-order moments, M, define the void's center
382 of mass (centroid). Second-order moments, I, define the inertia (or covariance) matrix, with
383 eigenvectors representing the ellipsoid axes orientations. Major, minor and medium ellipsoid radii,

384 r, were computed as $r = \sqrt{5|\text{eigenvalue}|}$ from each corresponding eigenvalue of the inertia
385 matrix (Ollion et al., 2013).

2.5.3 *Crack network scaling exponents and correlation length*

387 To find evidence for the type of phase transition undergone by each sample, we obtained
388 the following indicators of critical point behavior: the correlation length, ξ (linear dimension of
389 the largest void), the void size exponent, β, and the void separation exponent, or correlation
390 dimension, D. These time-dependent parameters are equivalent to those commonly used to
391 quantify the evolution of seismicity from acoustic monitoring (Aki, 1965; Sykes and Jaumé, 1990;
392 Bufe and Varnes, 1993; Sornette and Sammis, 1995; Turcotte, 1997; Ouillion and Sornette, 2000;
393 Zöller et al., 2001; Kagan, 2002; Sammis and Sornette, 2002; Tyupkin and Giovambattista, 2005).
394 In rock deformation studies (e.g., Moura et al., 2005; Lei and Satoh, 2007), these parameters have
395 been similarly inferred from the amplitudes and locations of acoustic emissions (AE). In particular,
396 the inter-crack distance inferred from AE is a key parameter that controls the failure time and
397 hence the accuracy of failure-time forecasts (Vasseur et al., 2017).

398 In this study, we obtained ξ, β and D directly from the evolving population of micro-cracks
399 in the µCT data, rather than indirectly from AE. We used void volume as a metric for void size
400 and estimated inter-void distances (void separation) from the distribution of points defined by
401 ellipse centroids. We obtained void volumes, V_i, and centroids (Text S1b in SI) directly from the
402 Label Analysis module in Avizo™, and then computed Euclidean lengths, L_i, between centroids.

403 We obtained maximum likelihood estimates of the void size exponent, β, from the
404 frequency-volume distribution in each µCT sub-volume. We tested three different but related
405 models often used to describe the seismic moment distribution in seismicity (Kagan, 2002 – full
406 details of this procedure are given in Text S3 in SI):

407 (i) GR: the Pareto distribution (a pure power law, equivalent to the Gutenberg-Richter
408 distribution) with cumulative complementary (survivor) function $\Phi(V) = (V_t/V_i)^\beta$ for
409 $V_t < V_i < V_{max}$, where V_i is volume of each individual void and V_{max} is the upper bound
410 (maximum) void volume in the distribution.

411 (ii) TRP: the truncated Pareto distribution (similar to the GR but showing a power-law taper
412 in the tail towards V_{max}), with $\Phi(V) = [(V_t/V_i)^\beta - (V_t/V_c)^\beta]/[1 - (V_t/V_c)^\beta]$ for $V_t <$
413 $V_i < V_c$, where V_c is the tapering corner volume of the distribution.

414 (iii) TAP: the tapered Pareto distribution (equivalent to the modified Gutenberg-Richter
415 relation which shows an exponential taper in the tail towards V_{max}), with $\Phi(V) =$
416 $(V_t/V_i)^\beta \exp[(V_t - V_i)/V_c]$ for $V_t < V_i < \infty$.

417 We defined a correlation length, $\xi = \sqrt[3]{V_{max}}$ for the pure power-law model or $\sqrt[3]{V_c}$ for the
418 truncated models. The completeness volume, V_t, is the smallest void volume at which 100% of
419 voids in a space-time volume are detected (Rydelek and Sacks, 1989; Woessner and Wiemer,
420 2005; Mignan and Woessner, 2012), and is equivalent to the threshold of completeness in
421 seismicity data. We obtained V_t from the maximum curvature method (Roberts et al., 2015), i.e.,
422 from the peak of the incremental frequency-volume distribution. This method is appropriate for
423 the sharp-peaked distributions seen in our data (Figure S1 in SI). In both samples, the number of
424 voids with $V \geq V_t$ exceeded 200, which is the minimum catalogue size required for reliable
425 estimation of β (Roberts et al., 2015). We used a modified Bayesian Information Criterion (BIC)

426 (Leonard and Hsu, 1999; Bell et al., 2013a) to find the most appropriate model (see Text S3 for
427 full details of the calculation, and Figure S2 in SI for the full results) thus obtained the most likely
428 values of β and ξ for each distribution. The BIC is more appropriate for distributions of large
429 sample populations investigated here than the AIC, and the results can be compared more directly
430 with previous work (Bell et al., 2013a).

431 To distinguish the type of phase transition, i.e., whether or not ξ followed an inverse power-
432 law acceleration to failure, we fit the data by non-linear least-squares regression to an inverse
433 power-law model of the form: $y = k(x_p - x)^{-p}$, where x_p is the predicted value of the control
434 parameter x at failure, k is a scaling factor and p parameterizes the rate acceleration of y, all
435 determined by non-linear regression. The point of failure, x_p, is defined by a mathematical
436 singularity as $y \to \infty$. This is directly analogous to the approach to a critical point in a second order
437 phase transition for the correlation length (Equation 1). It is also equivalent to material failure
438 forecasting approaches based on the Time-Reversed Omori Law for aftershock decay (e.g., Voight,
439 1988; Cornelius and Voight, 1994; Utsu et al., 1995; Kilburn and Voight, 1998; Kilburn 2003;
440 Smith et al., 2009; Bell et al., 2013b; Vasseur et al., 2015; 2017). We used stress as the control
441 parameter instead of time because the stepped loading procedure that we conducted precludes
442 realistic temporal rate estimates. Importantly, this model makes no *a priori* assumptions about any
443 of the parameters. The predicted failure stress, σ_p, is what would be available in real time, rather
444 than the observed failure stress, σ_c. By estimating σ_p independently, we can quantify any
445 systematic error in its estimation by comparing it to the observed failure stress, and hence quantify
446 any bias in a potential forecasting scenario. We used a trust region algorithm to minimize the
447 residual sum of squares between the observed data and the model (see Text S5 in SI for details).
448 We also tested an exponential model $y = h \exp(qx)$ as an alternate hypothesis. We cannot use a
449 simple criterion such as r^2 alone to determine the relative goodness of fit because the competing
450 hypotheses have different degrees of freedom, so we used the corrected Akaike Information
451 Criterion ($AICc$ – see Text S2 in the Supporting Information for details of the calculations). It is
452 based on the residual sum of squares, and is considered more robust than r^2 alone because it takes
453 into account the number of parameters in the model, penalizes models with more parameters and
454 can be used to determine the relative likelihood of the models given the data.

455 We obtained the two-point fractal dimension, D, from the relation $P(L_i) \sim L_i^{D-1}$ (Turcotte,
456 1997), where $P(L_i)$ is the incremental probability distribution of the inter-void lengths, L_i (see
457 Text S4 in the SI for more detail). The exponent, $D_{inc} = D - 1$, of $P(L_i)$ in the identified power-
458 law region, $30 < L_i < 1350$ μm, was obtained from a linear regression in log-log space (Figure
459 S3 in the SI). D is then $D_{inc} + 1$. If $D < 3$, voids are clustered spatially but as $D \to 3$ they
460 become volume-filling, and therefore less clustered (Robertson et al., 1995).
461

462 **3 Results: Micro-fracture network evolution**

463   Here we present our 4D observations of the evolving segmented fracture network in each
464 sample, together with the distributions of micro-crack orientations. This is followed by results
465 from our quantitative analysis of the fracture network. We first show the influence of heterogeneity
466 on the evolution with strain of (i) stress, porosity and the number of voids, and (ii) void geometry,
467 which reveals how the initial, small anisotropy of the crack network increased in the lead-up to
468 failure. Following this, we test our hypothesis regarding the type of phase transition undergone by
469 each sample by showing the transition to failure of the correlation length as a function of stress.
470 Finally we present the evolution with strain of the correlation length and the scaling exponents of
471 void size and separation. For the purposes of testing our hypothesis and for clarity of presentation
472 we have analyzed data up to failure but not beyond.

473   **3.1**   **4D observations of micro-fractures and their orientations**

474   The spatial evolution of micro-cracks differs significantly between the two samples (Figure
475 4 and Figure 5). Although the untreated sample appeared to fail along a localized shear fault
476 (Figure 4P), pre-failure damage accumulated in a spalling pattern of radial damage zones sub-
477 parallel to σ_1 (Figure 4F-O). Conversely, the heat-treated sample failed along a localized shear
478 fault, inclined at 30° to σ_1, along which pre-failure damage had already accumulated (Figure 5K-
479 P). In both samples, the localized damage zones consisted mainly of shear and axial micro-
480 fractures oriented between 5° and 30° to σ_1 (Figure 6a,b) with bridging ligaments. Local fracture
481 aperture increased as fractures propagated within the localized zones of damage.

482   In the untreated sample, damage localization (established visually from the segmented CT
483 volumes in Figure 4) first occurred along four narrow zones simultaneously (orange ellipses in
484 Figure 4F) at 1.37% strain and 64% of the failure stress, σ_c, (Table 3). Damage was concentrated
485 along these zones until further radial zones developed on the other side of the sample (pink ellipses
486 in Figure 4J) at 85% σ_c. It is not clear exactly how the eventual fault developed because the sample
487 failed before the next scheduled image time. The post-failure μCT sub-volume (Figure 4P)
488 indicates that slip occurred along a plane not previously localized and located slightly above where
489 the radial damage had accumulated, which is consistent with the sudden, abrupt nature of the
490 failure inferred from the stress-strain data (Section 3.2.1). However, close to peak stress (97% σ_c;
491 Figure 4O) cracks had begun to localize along a shear zone that was above and formed from the
492 tip of some of the radial damage zones, and was conjugate to the eventual fault plane.

493   In the heat-treated sample, damage localization (established visually from the segmented
494 CT volumes in Figure 5) first occurred along a shear zone conjugate to the eventual fault plane
495 (orange ellipse Figure 5H) at 1.24% strain and 72% σ_c (Table 4). Damage progressively
496 concentrated along this plane until localization around the incipient fault plane became apparent
497 (pink ellipse in Figure 5K) at 90% σ_c and 1.38% strain; the same amount of strain as the initial
498 localization in the untreated sample. Fracture nucleation and propagation within the initial damage
499 zone then stopped, continuing instead along this more favorably-oriented zone until failure. This
500 flip in orientation between two optimally-oriented, conjugate, shear planes has previously been
501 seen by Lennartz-Sassinek et al. (2014). Here it coincides with reduced sample stiffness and strain
502 hardening inferred from the stress-strain data (Section 3.2.1).

503   Microcrack dips, ϕ, became progressively more vertical with increasing stress in both
504 samples (Figure 6a,b), indicating the preferential nucleation of tensile cracks. These cracks formed

505   en-echelon (Tapponnier and Brace, 1976; Kranz, 1979; Olson and Pollard, 1991; Reches and
506   Lockner, 1994) and wing-crack *(*Fairhurst and Cook, 1966; Nemat-Nasser and Horii, 1982; Horii
507   and Nemat-Nasser, 1985; 1986; Ashby and Hallam, 1986; Nemat-Nasser and Obata, 1988; Ashby
508   and Sammis, 1990) arrays (Figure 7), concentrated in the heat-treated case at the tip of the
509   propagating fault zone. All radial damage zones in the untreated sample grew in this manner
510   immediately after their initial localization (Figure 4F onwards). In contrast, this process occurred
511   only in the heat-treated sample during localization around the eventual fault plane (Figure 5L
512   onwards), not during the initial localization around the unfavorable conjugate. En-echelon and
513   wing-crack arrays formed at 1.45±0.01% strain in both samples (Figure 4G and Figure 5L). At
514   this point the untreated sample was only at 70% σ_c, compared to 90% for the heat-treated sample.

515   One advantage of the 3D sampling enabled by µCT imaging is that we can test the null
516   hypothesis that the initial sample porosity is isotropic. The optimal strikes of the segmented voids,
517   θ, show a predominant orientation in the initial porosity in both samples (Figure 6c,d). This starting
518   anisotropy was more pronounced in the heat-treated sample than in the untreated sample
519   (33.0±15.1% compared with 14.3±11.8% - see Table S1 in SI). Overall, anisotropy in the void
520   strike increased steadily throughout deformation in the heat-treated sample but remained
521   approximately constant in the untreated sample (Table S1 in SI). The strike of the eventual fault
522   closely followed this pre-existing anisotropy in both samples, but to a much greater degree in the
523   heat-treated sample. In the untreated sample, although the distribution peaks and troughs broaden
524   as the radial zones localized, the strike of the post-failure fault was oriented within 30° of the initial
525   preferred strike orientation (Figure 6c). In the heat-treated sample, the strike of the emerging fault
526   plane tracked the orientation of the initial crack porosity anisotropy almost exactly (Figure 6d),
527   while the distribution of peaks and troughs remained stationary, and became more defined, as the
528   damage zone localized.

529   Stereonet depictions (Figure 8) of the void orientations (poles to planes) projected along
530   the axial direction (σ_1) confirm these observations, showing a predominant strike parallel to the
531   pre-existing porosity in both samples, followed by the development of mainly vertical cracks at
532   localization, in line with our visual examination. These cracks initially cluster along the pre-
533   existing strike in both samples but become increasingly distributed in the untreated sample (blue
534   stereonets) during yield and approaching failure, with failure occurring along a fault offset by
535   around 30° to the pre-existing strike. Conversely, in the heat-treated sample (orange stereonets),
536   these vertical cracks cluster increasingly along the pre-existing strike throughout deformation.
537   Closure of some shallow-dipping voids is seen in both samples.

538   In the time-lapse video of the untreated sample in the x, y projection (Video S1 in the SI),
539   the first axial fracture initiated at a spot on the sample edge close to the bottom of the sample,
540   below and on the outside of a region of concentrated porosity. Further localization occurred
541   simultaneously along vertical zones distributed radially around the sample, which appear to have
542   grown preferentially into the sample before propagating vertically as crack segments linked up.
543   Approaching peak stress, an array of micro-cracks with varying orientations formed around the
544   region of concentrated initial porosity, bridging three radial zones in a curved damage zone. The
545   same process occurred again at 97% σ_c, bridging four radial zones adjacent to the previous three,
546   but in a conjugate orientation. This bridging fault propagated up the sample (Video S2 in the SI –
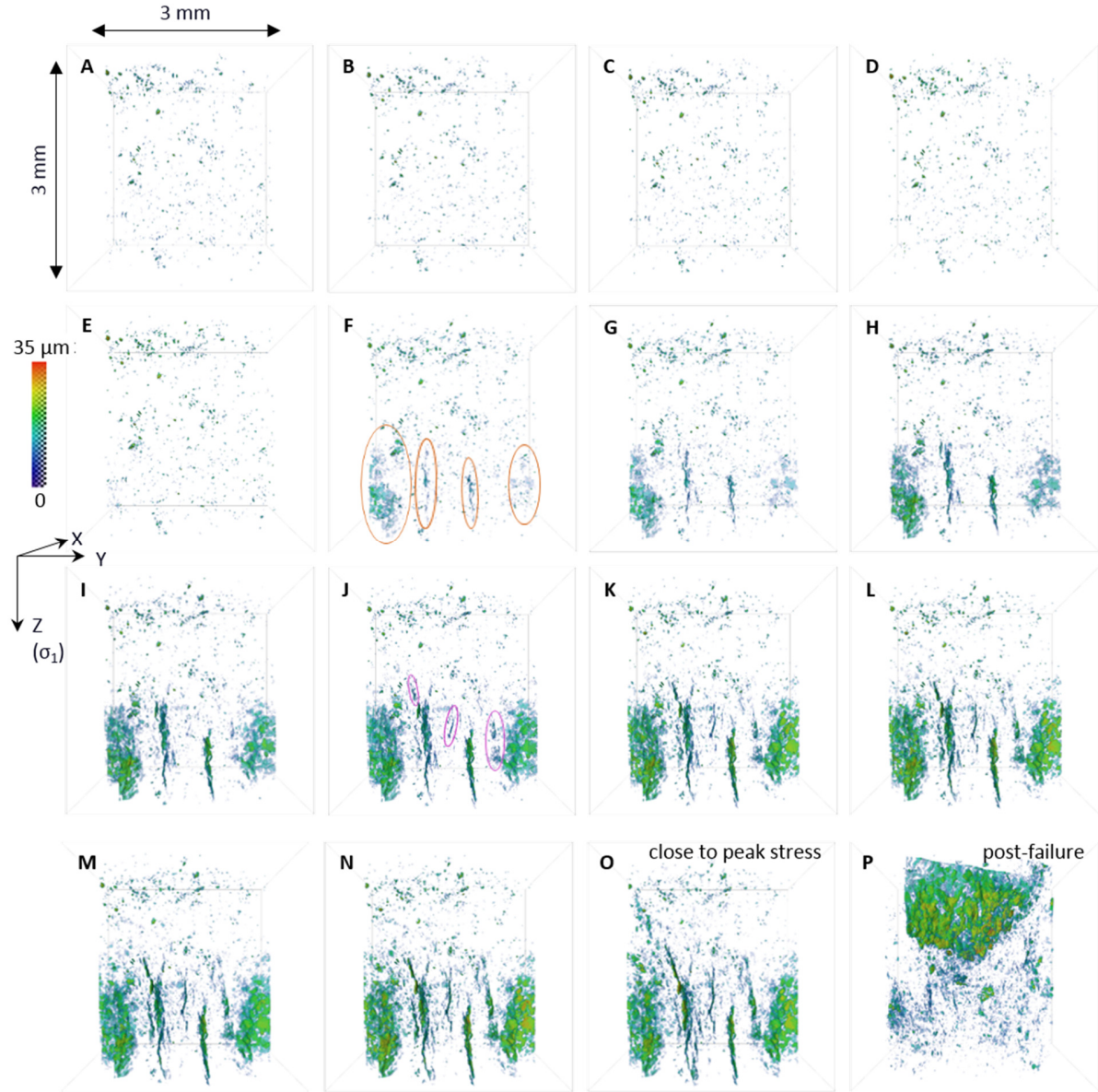547 y, z projection), at a different strike to the post-failure fault.

548   Time-lapse video of deformation in the heat-treated sample in the x, y projection (Video
549   S3 in the SI) shows that localization initiated within the sample, not at the boundary, on the site of

550 a pre-existing void, precisely as anticipated by Griffith (1921, 1924). Subsequent micro-cracks
551 that localized along the damage zone nucleated between the initial site and the sample edge. The
552 emerging fault plane initiated at the sample boundary and grew horizontally into the sample, as
553 subsequent micro-cracks localized along it, before propagating down the sample parallel to the z, x
554 plane (Video S4 in the SI – y, z projection). Simultaneously, micro-cracks localized on the
555 opposite side of the sample along the same strike as the initial, arrested damage zone. As
556 deformation continued and the sample reached peak stress, micro-cracks nucleated in the center of
557 the sample. These cracks joined the optimally-oriented damage zone to the conjugate damage zone
558 on the other side of the sample, resulting in a curved shear zone, consisting of arrays of micro-
559 crack segments linked by bridges of intact rock, along which the sample failed.

Table 3: Differential stress, σ, and axial strain, ϵ, for each µCT sub-volume in the untreated sample [ACfresh02]. Letters A-P refer to the image volumes shown in Figure 4. Localization first appeared in scan F along several vertical zones distributed radially around the sample. Additional zones localized in scan J but scan P shows that failure occurred along an unrelated shear fault.
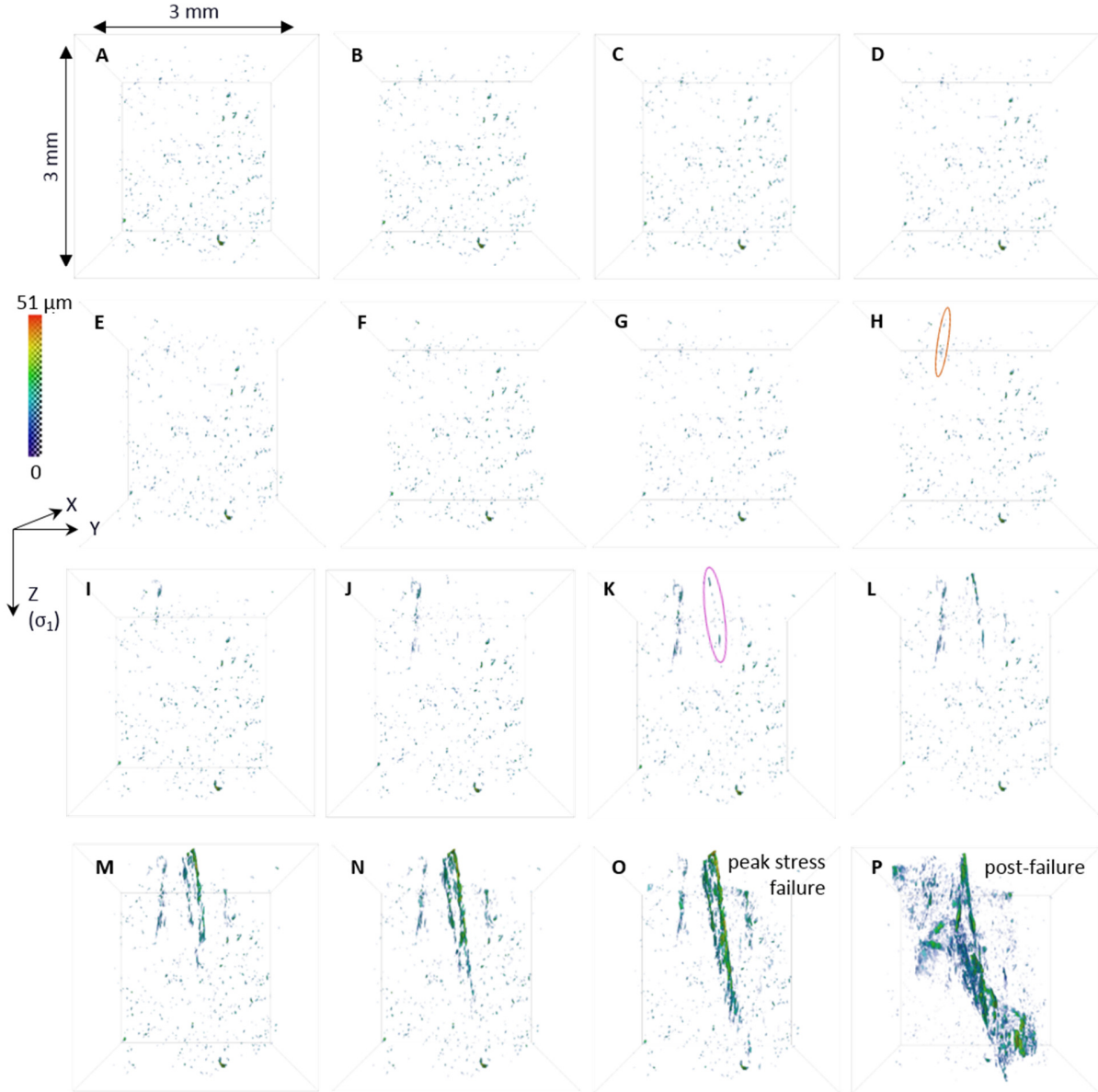
ACfresh02	A	B	C	D	E	F	G	H	I	J	K	L	M	N	O	failure	P
σ (MPa)	7	41	60	79	97	116	126	135	144	154	158	163	168	172	177	182	127
ϵ (%)	0.00	0.56	0.81	1.00	1.18	1.37	1.46	1.62	1.71	1.77	1.84	1.87	1.93	1.99	2.08	-	25.79

Figure 4: Projection in the y, z plane of segmented microfractures for the untreated sample [ACfresh02]. Orange ellipses show the onset of localization, pink ellipses indicate formation of additional localized zone, completing the radial pattern. Letters refer to the stress-strain steps in Table 3. Color-coding shows the local fracture aperture at each voxel. See Figure S5 in SI for zip file of high resolution images.

Table 4: Differential stress, σ, and axial strain, ϵ, for each μCT sub-volume in the heat-treated sample [ACHT01]. Letters A-P refer to the image volumes shown in Figure 5. Localization was first seen in scan H along a shear zone that subsequently arrested when microcracks localized along a more favorably-oriented damage zone in scan K, along which the sample eventually failed.
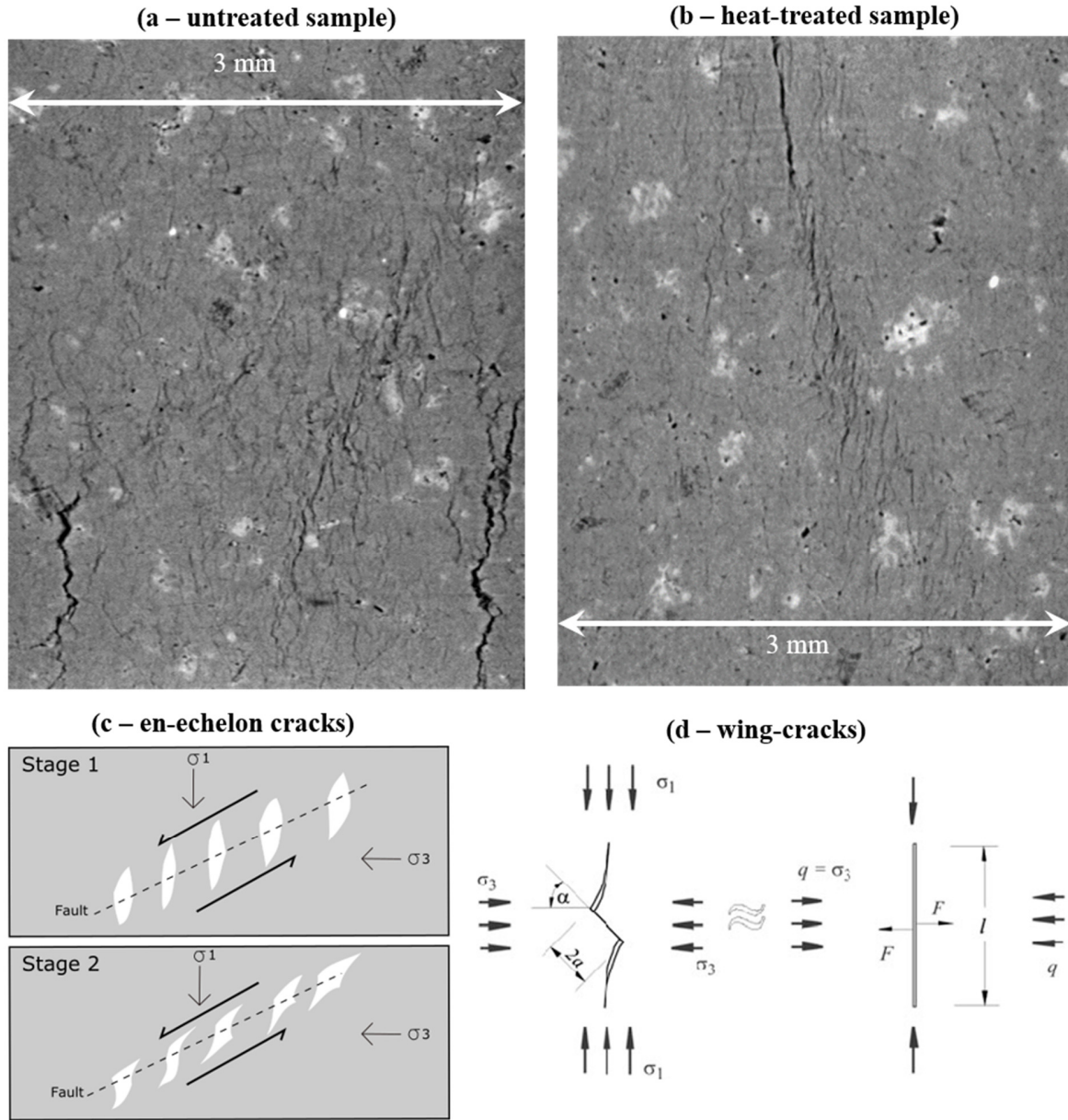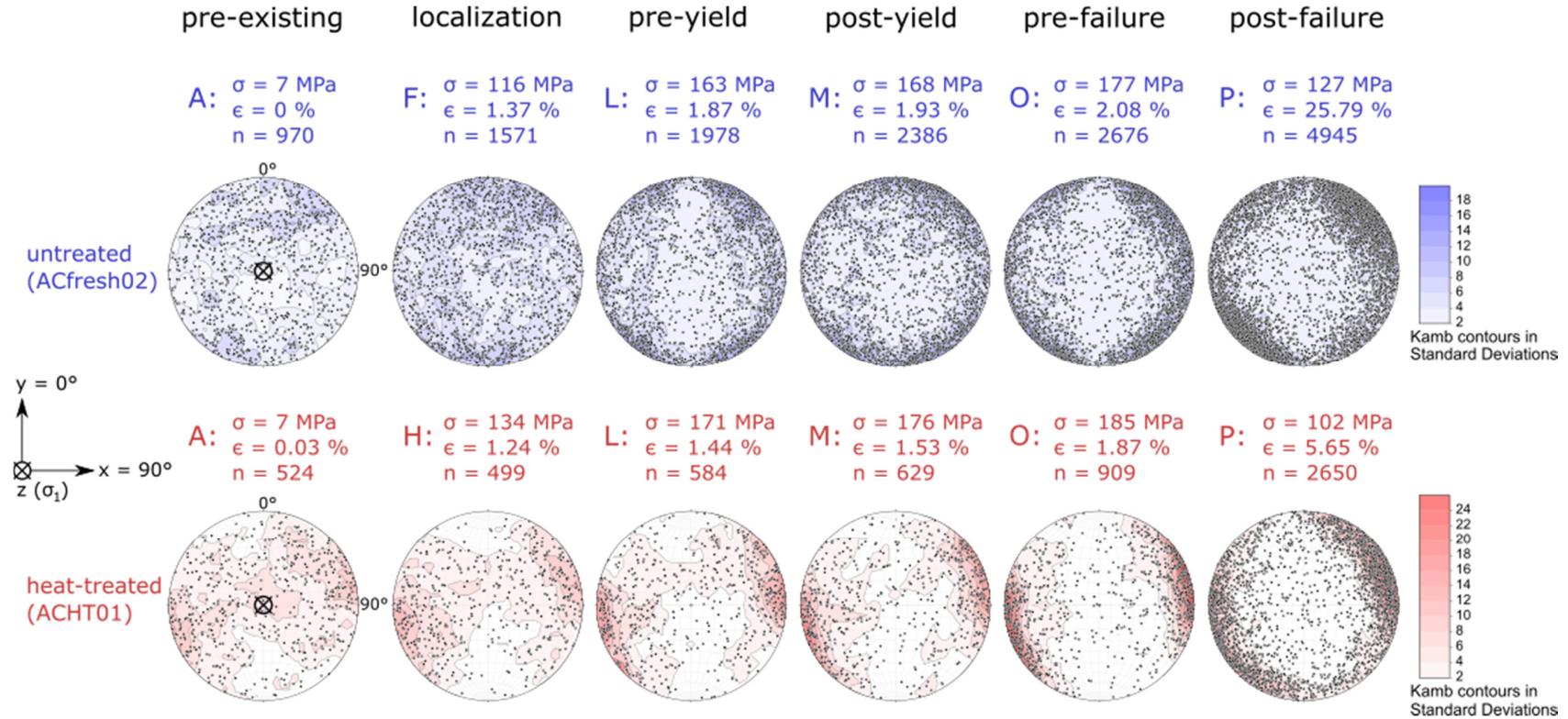
ACHT01	A	B	C	D	E	F	G	H	I	J	K	L	M	N	O (failure)	P
σ (MPa)	7	41	59	78	97	115	125	134	153	162	167	171	176	181	185	102
ϵ (%)	0.03	0.35	0.63	0.84	0.92	1.04	1.09	1.24	1.30	1.38	1.41	1.44	1.53	1.73	1.87	5.65

Figure 5: Projection in the y, z plane of segmented microcracks for the heat-treated sample [ACHT01]. Orange ellipse indicates the onset of damage localization, pink ellipse indicates localization along the emerging fault plane. Letters refer to the stress-strain steps in Table 4. Color-coding shows the local fracture aperture at each voxel. See Figure S6 in SI for zip file of high resolution images.

Figure 6: Void (**a,b**) dip ϕ and (**c,d**) strike θ probability distributions at each strain increment for (**a,c**) the untreated sample and (**b,d**) the heat-treated sample, calculated using the object-based best-fitting ellipsoid approach. Inset shows the measured angles with respect to the principal stress axes: $\phi = 90°$ is parallel to the z-axis, while $\theta = 0°$ is parallel with the y-axis. Labels on the dip distributions show the angles at which different damage mechanisms are prevalent. Strike distributions are normalized to the minimum $P(\theta)$ of the starting porosity. Blue distributions overlaying the rest are post-failure.

Figure 7: Slice through the sample in the y, z projection showing in (**a**) the untreated sample close to peak stress (Figure 4O) and (**b**) the heat-treated sample at peak stress (Figure 5O) the formation of tensile (**c**) en-echelon (Olson and Pollard, 1991; Thomas and Pollard, 1993) and (**d**) wing-cracks (Fairhurst and Cook, 1966; Fig. 15 in Damjanac and Fairhurst, 2010).

Figure 8: Stereonet projection of void ellipsoid orientations (poles to planes) projected down the loading axis (i.e., in the x, y plane) for both samples. Letters refer to the stress-strain steps for the untreated (Table 3 and Figure 4) and the heat-treated (Table 4 and Figure 5) samples. Clustering contours were calculated from uniform kernel density estimation to show significant departures from a uniform distribution (Kamb, 1959). Kernel radius, $r = 3/\sqrt{\pi(9 + n)}$, where n is the number of data points. Contour intervals are given as a multiple of the standard deviation to emphasize the statistical significance of the number of points falling into each kernel (Haneberg, 2004). In the untreated sample, strikes were dominated by the pre-existing porosity until scan F, when micro-crack localization initiated along the steeply dipping, radially distributed zones (orange ellipses in Figure 4). The radial pattern became increasingly symmetrical around the sample throughout the rest of the experiment as these zones propagated and as micro-cracks localized along new zones (pink ellipses in Figure 4). In the heat-treated sample, strikes were dominated by the pre-existing porosity throughout deformation, although the initial localized damage zone observed at scan H (orange ellipse in Figure 5) was conjugate to the eventual fault zone seen at scan J (pink ellipse in Figure 5).

606 ## 3.2 Evolution of specimen and microcrack characteristics with strain

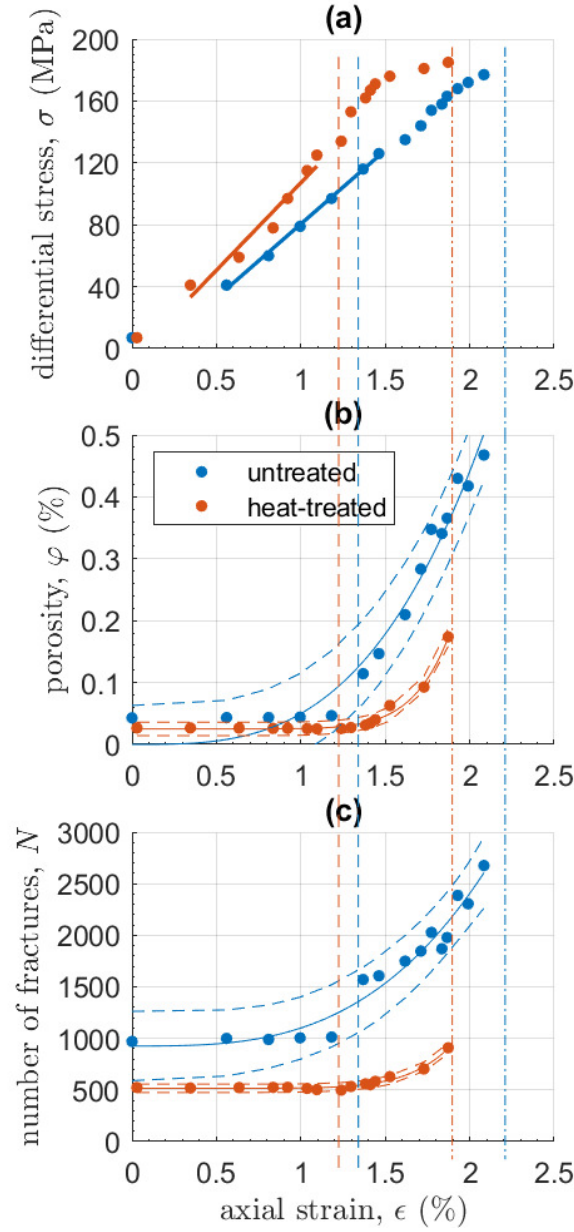607 ### 3.2.1 Stress, porosity and the number of voids

608 Both samples had a similar stiffness early on (Figure 9a) but the heat-treated sample
609 became stiffer at 0.84% strain when the number of voids decreased slightly (Figure 9c). This is
610 consistent with compaction of the compliant thermal microcracks. The onset of localization, as
611 determined visually from the CT volumes, is evident in both samples as a yield point in the stress-
612 strain curve; at 1.37% strain and 1.24% in the untreated (Figure 4F) and heat-treated (Figure 5H)
613 samples respectively. Further yielding occurred once the damage zone propagated at 95% σ_c in
614 the heat-treated sample (Figure 5M), but only from 97% σ_c in the untreated sample (Figure 4O).

615 The heat-treated sample had lower pre-existing porosity than the untreated sample
616 ($\varphi_{0\ HT} = 0.62\varphi_{0\ UT}$) and fewer but slightly larger voids ($N_{0\ HT} = 0.54N_{0\ UT}$), with half the
617 number of voids accounting for two-thirds of the porosity seen in the untreated sample (Figure
618 9b,c). However, this observation only accounts for voids visible above the detection threshold of
619 the segmentation algorithm (a void volume of 3000-4000 μm^3 – see Section 3.3.1), and does not
620 include unresolved nano-scale thermally-induced cracks. The observed differences may be
621 accounted for by natural sample variation within these very small samples and/or some void
622 closure from thermal expansion during the heat-treatment.

623 Both samples showed a ten-fold increase in porosity, φ, over the duration of their respective
624 deformation experiment (Figure 9b), but only a two-fold increase in the total number of voids, N,
625 in the heat-treated sample, compared with a nearly three-fold increase in the untreated sample
626 (Figure 9c). This indicates that crack nucleation was more dominant in the untreated sample,
627 compared with crack growth in the heat-treated sample. The untreated sample showed no evidence
628 of compaction in the early stages of deformation and the onset of localization (Figure 4E-F) is
629 evident as a large jump in N of 600 voids at 1.37% strain, and a corresponding three-fold increase
630 in φ (Figure 9). Conversely, in the heat-treated sample a small decrease in N of approximately 50
631 voids provides evidence for some early compaction due to void closure, although this equates to
632 only a tiny proportion (0.005%) of φ_0. This was associated with the closure of some optimally
633 oriented (shallow dipping) voids prior to localization (Figure 8 – orange stereonets). The onset of
634 localization is evident as a minimum in both φ and N at 1.24% strain (Figure 5H) and both
635 variables exceeded their initial values when the optimally oriented damage zone localized (Figure
636 5K). Once localization initiated, both samples showed an overall acceleration towards failure in
637 both φ and N. However, in the untreated sample there were two occasions where the acceleration
638 was temporarily arrested. The first of these corresponded to the propagation of new localized zones
639 (Figure 4J), while the second corresponded to the change in orientation of the bridging zone
640 (described in Section 3.1). The heat-treated sample showed a slight slow-down in acceleration that
641 corresponded to the nucleation of new micro-cracks between the two ends of the eventual fault
642 (described in Section 3.1), followed by a final acceleration immediately before dynamic rupture.

643 In both samples the evolution of both φ and N with strain is best described with simple
644 power-law models (Figure 9b,c); i.e., they have the lowest $AICc$, (Tables S2 and S3 in SI). The
645 exponent is 3.1 for both variables in the untreated sample, compared with 8.8 and 7.7 for φ and N
646 respectively in the heat-treated sample, showing an acceleration towards failure that was almost
647 three times faster in the heat-treated sample than the untreated one. These exponents also show
648 that the acceleration in N accounted for all of the acceleration in φ in the untreated sample,

649 confirming that crack nucleation was the dominant damage mechanism throughout deformation,
650 whereas in the heat-treated sample, the acceleration in N did not completely account for all of the
651 acceleration in φ, confirming that crack growth played an increasingly important role closer to
652 failure.

653

Figure 9: Evolution of (**a**) differential stress, σ, (**b**) porosity, φ and (**c**) the number of
segmented voids, N, with increasing axial strain, ϵ for the untreated sample (blue circles) and the
heat-treated sample (orange circles). Dash-dot lines show the strain at which each sample failed,
while dashed lines show the onset of damage localization as seen the μCT volumes (Figure 4 and
Figure 5). Solid lines in (**a**) show the region of data used to calculate the Young's moduli (11.3
and 9.5 GPa respectively). Solid lines in (**b**) and (**c**) show the preferred simple power-law models
with 95% confidence intervals shown as dashed lines; see text for exponents.
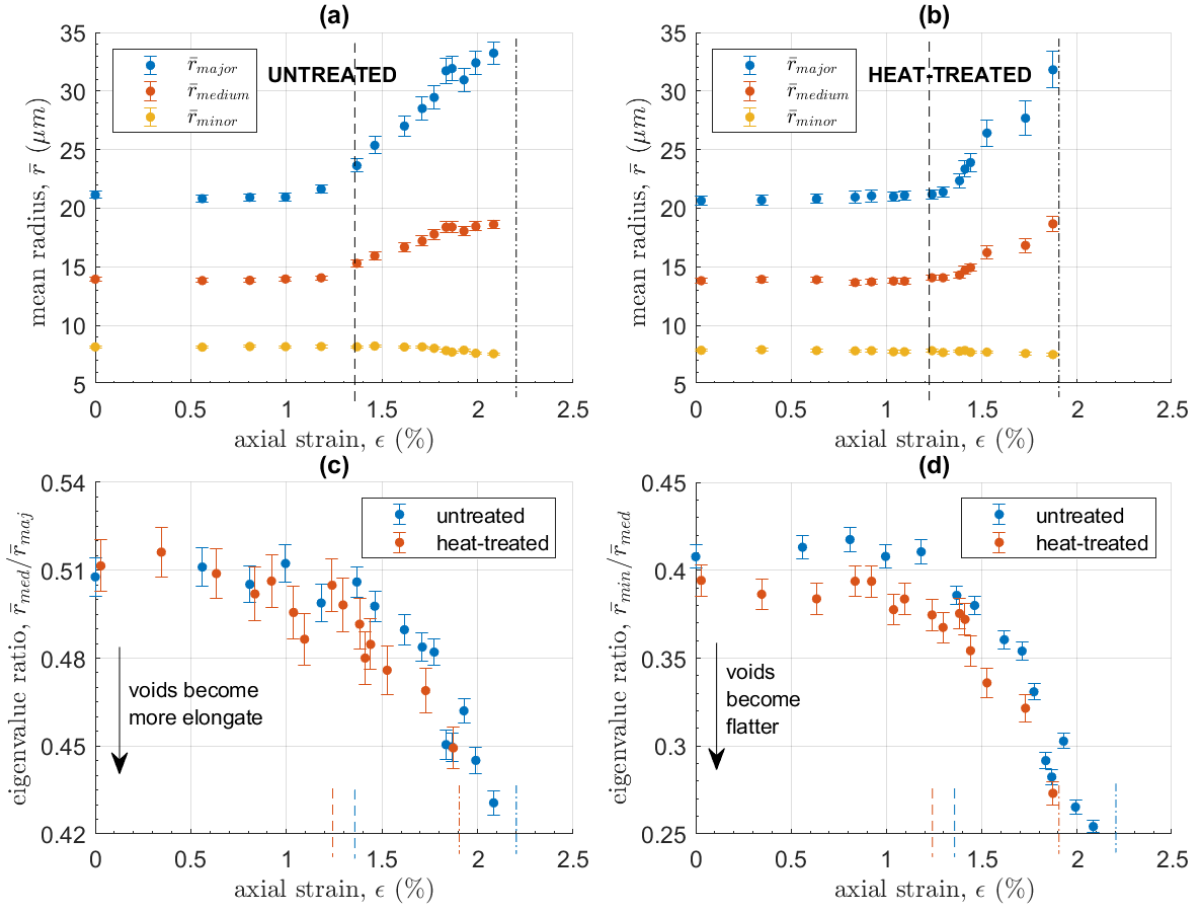
661   *3.2.2   Micro-crack geometry*

662   To establish empirically how the micro-crack geometry evolves with increasing
663   deformation, we present the variation with strain of the mean value of the major, minor and
664   medium ellipsoid radii from the population of voids in each μCT sub-volume (Figure 10a,b). We
665   also show the mean ellipsoid eigenvalue ratios, used to infer the evolution of void aspect ratio
666   (Figure 10c,d). We present two ratios: (i) the smallest to the medium eigenvalue of the covariance
667   matrix (Section 2.5.2 and Text S1b in SI), where flatter objects have smaller values, and (ii) the
668   medium to the largest eigenvalue, where more elongated objects have smaller values.

669   Corresponding mean void radii, $\bar{r}$, were about the same size in both samples. In the
670   untreated sample (Figure 10a) $\bar{r}_{major}$ and $\bar{r}_{medium}$ (blue and orange circles respectively) began to
671   increase at the onset of localization (Figure 4F). In the heat-treated sample (Figure 10b) they began
672   to increase as micro-cracks localized along the optimally oriented damage zone (Figure 5K), after
673   the onset of localization. In both samples, r_{major} were oriented approximately parallel to the strike
674   of the eventual fault plane (Figure 6c,d), with their mean values, $\bar{r}_{major}$, increasing more quickly
675   than $\bar{r}_{medium}$, showing that micro-cracks grew twice as fast along strike (i.e., perpendicular to σ_1)
676   than down dip, becoming more elongate as deformation progressed (Figure 10c). Voids in the heat-
677   treated sample were marginally flatter than those in the untreated sample, with voids in both
678   samples becoming flatter as failure approached (Figure 10d). This implies that the scaling of crack
679   growth, while scale-invariant in length, may be self-affine (variable aspect ratio) rather than self-
680   similar (constant aspect ratio). The down-dip extent ($\bar{r}_{medium}$) increased from 2.5 to 4 times the
681   crack aperture ($\bar{r}_{minor}$ – yellow circles). In the heat-treated sample, this was due to continued crack
682   growth down dip relative to a constant crack aperture (Figure 10b). However, in the untreated
683   sample, crack growth down dip stopped altogether close to failure and a small decrease in aperture
684   accounted for the voids becoming flatter (Figure 10a). Growth along strike also stopped (within
685   error), and the continued increase in the number of cracks at this stage (Figure 9c) confirms that
686   nucleation of new cracks accounted for almost all the porosity generation close to failure in this
687   sample.

688   In summary, the average growth pattern of individual micro-cracks is independent of
689   heterogeneity in the early stages of localization. The behavior changes close to failure, with
690   continued crack growth in the heat-treated sample accounting for the faster acceleration in porosity
691   than void number, while crack growth in the untreated sample was effectively halted in favor of
692   crack nucleation, which accounted for the entire acceleration in porosity and void number as failure
693   approached.

694

Figure 10: (**a,b**) Evolution with strain of the mean void ellipsoid radii, $\bar{r}_{major}$ (blue circles), $\bar{r}_{medium}$ (orange circles) and $\bar{r}_{minor}$ (yellow circles), for the (**a**) untreated and (**b**) heat-treated samples. (**c,d**) Evolution of mean void eigenvalue ratios (**c**) $\bar{r}_{med}/\bar{r}_{maj}$ and (**d**) $\bar{r}_{min}/\bar{r}_{med}$ with strain in the untreated (blue circles) and heat-treated (orange circles) samples. Voids become flatter or more elongate as the respective ratio $\rightarrow 0$. Error bars show the standard error of the mean in each µCT sub-volume. Dash-dot lines show the failure strain for each sample while dashed lines show the onset of localization as seen in the µCT volumes.
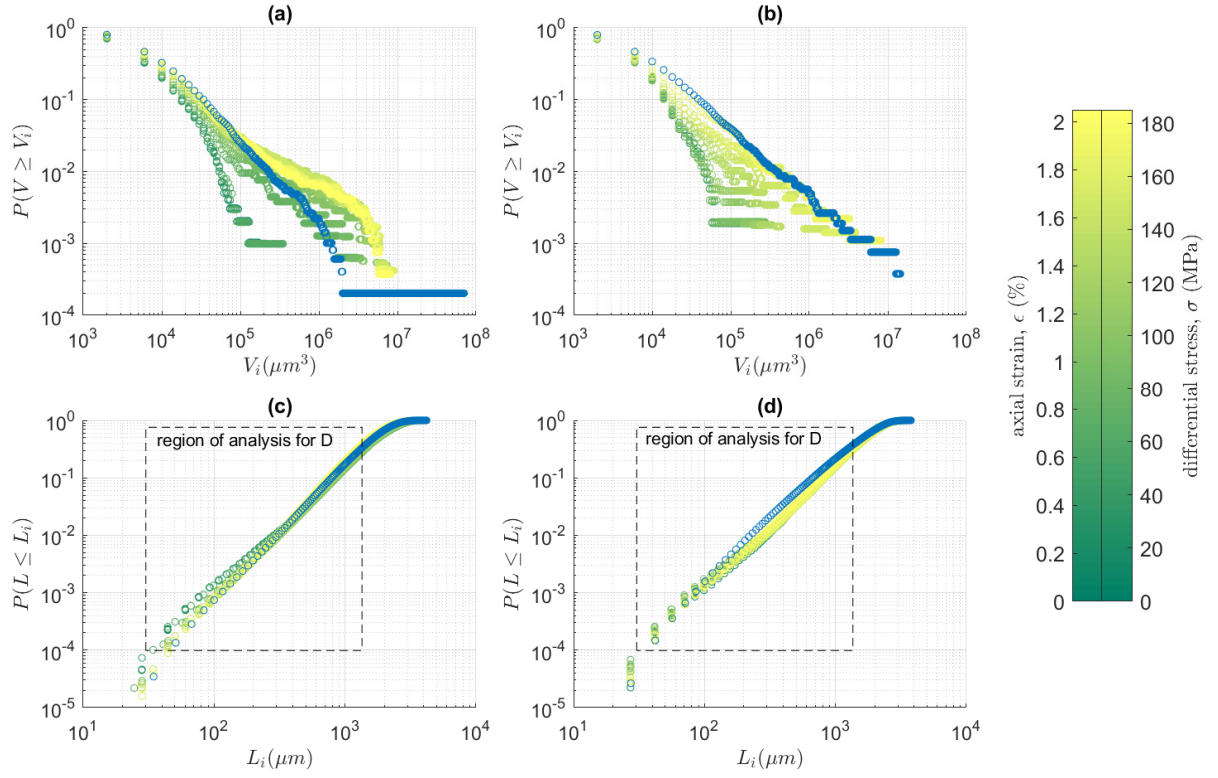
702

3.3 Evidence for phase transition style

To establish the type of phase transition undergone by each sample, we present the evolution to failure of the correlation length and the scaling relations as a function of both differential stress σ and axial sample strain ϵ. Renard et al. (2018) argue that stress is a stronger control variable than strain, but strain is usually the only directly-observable control parameter in real Earth applications. We first present the scaling relationships for void volume and inter-void length, and then show how the correlation length, ξ (linear dimension of the largest void) evolves as a function of stress. We then analyze the evolution of ξ, β and D (the void volume and inter-void length exponents respectively, defined in Section 2.5.3) as a function of strain.

3.3.1 *Microcrack volume and inter-crack length distributions*

Both samples show an approximately power-law complementary probability distribution in void volume, V_i, (Figure 11a,b), with the proportion of larger voids increasing systematically with respect to strain and stress. Both samples also show an approximately power-law distribution in their inter-void lengths, L_i (Figure 11c,d), within a finite range, identified as $30 < L_i < 1350$ μm (close to half the sample diameter), with little apparent difference in the shape of the distributions as stress and strain increase. We can therefore define power-law scaling exponents β from the frequency-volume distributions and the correlation dimension D from the inter-void length distributions.
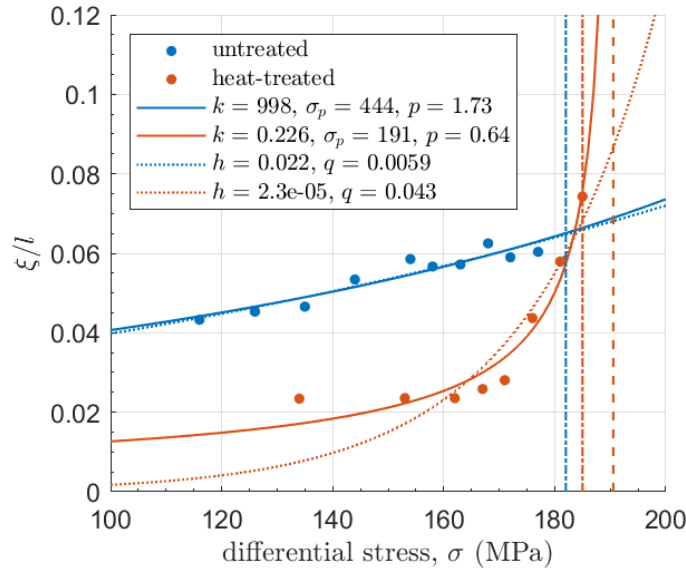
Values of completeness volume, V_t (defined in Section 2.5.3), ranged from 3000 to 4000 μm³, roughly equivalent to a void aperture of 14-16 μm. This is much larger than the theoretical detection threshold of half the pixel size (1.3 μm) consistent with under-sampling of very narrow cracks during segmentation. Void volumes in the untreated sample are best described (i.e., have the lowest BIC) by the truncated Pareto distribution (TRP) at the three earliest steps of deformation and then by the characteristic Pareto distribution (GR), with the transition between the two models occurring at 43% σ_c, two stages before the onset of localization (Figure S2 in the SI). In contrast, void volumes in the heat-treated sample are best described by the GR distribution throughout the experiment.

Figure 11: (**a,b**) Cumulative complementary probability distributions of void volumes, V_i, computed with a bin width of 4000 μm³, and (**c,d**) cumulative probability distributions of inter-void lengths, L_i, computed with 256 bins, at each increment of stress and strain in the (**a,c**) untreated and (**b,d**) heat-treated samples. As described in Section 2.5.3, we obtained maximum likelihood estimates for β from the cumulative complementary V_i data (see Figure S1 in SI) using the models of Kagan (2002), and fitted the incremental L_i data using linear regression in log-log space (see Figure S3 in SI) to find D, after Turcotte (1997). Blue distributions overlaying the rest are post-failure.

3.3.2 *An inverse power-law acceleration to failure?*

Parameters for an inverse power-law acceleration to failure for the normalized correlation length, ξ/l, were obtained for both samples (Figure 12), using data observed in segmented μCT volumes between Figure 4F-O and Figure 5H-O and the method described in Section 2.5.3. While an inverse power-law acceleration is commonly only distinguishable from an exponential acceleration within 10% of the singularity (Bell et al., 2013b), restricting the data to this region (stages L-O in the untreated sample and K-O in the heat-treated sample) would have left very few data points for the analysis. In the untreated sample the exponential and inverse power-law models are indistinguishable over the data range, and the predicted failure stress, σ_p, is far from the observed failure stress, σ_c. The likelihood that the inverse power-law model fits the data as well as the exponential model is just 3% (Table S5 in SI). Thus, it is impossible to define an accurate failure point in this sample. The sample failed abruptly, long before the predicted singularity, after an exponential acceleration in the correlation length. Conversely, in the heat-treated sample, σ_p is accurate to within 3% of σ_c, while the asymptote of the exponential model is further from σ_c. The likelihood of the exponential model fitting the data as well as the inverse power-law is 72% (Table S5 in SI), which although relatively high, is not significant (>95%). These differences are diagnostic of a first (abrupt) and second (continuous) order phase transition respectively (Figure 1), validating our hypothesis that, within the temporal resolution of our experiments, the transition to failure is first-order in the untreated sample and second-order in the heat-treated sample.

Figure 12: Evidence for an inverse power-law acceleration (solid lines) with respect to stress in the correlation length (normalized by the length of the analyzed sub-volume): $\xi/l = k(\sigma_p - \sigma)^{-p}$ in the heat-treated sample (orange), to a predicted failure stress, σ_p, within 3% of the observed failure stress, σ_c. This compares with the same model yielding a much poorer prediction in the untreated sample (blue), where $\sigma_p = 2.4\,\sigma_c$. Dotted lines correspond to the exponential model, $\xi/l = h\exp(q\sigma)$, which in the heat-treated sample is less likely and in the untreated sample is more likely than the inverse power-law model (the relative likelihood of each model is expressed in the main text and also in Table S5 in SI, along with the $AICc$ values). The dash-dot lines show σ_c for both samples and the dashed line shows σ_p for the heat-treated sample.
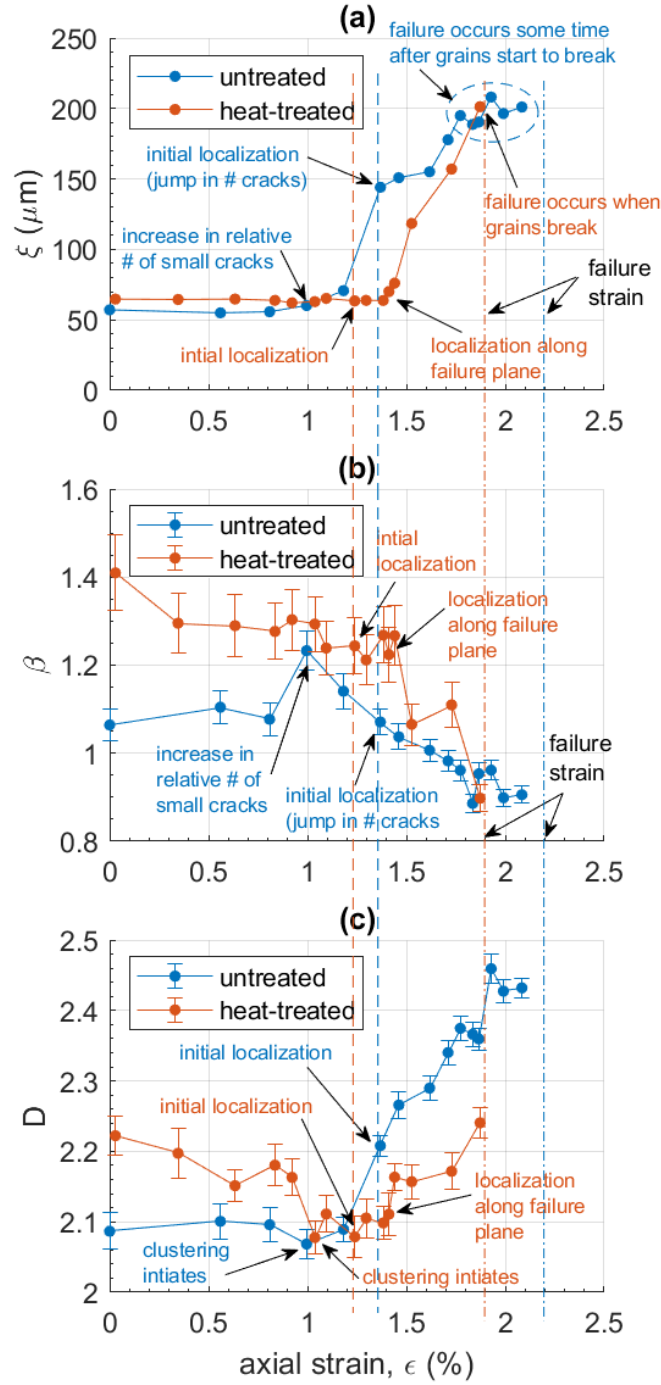
769   *3.3.3   Evolution of crack population metrics with respect to strain*

770   Both samples show a systematic increase in the correlation length ξ towards failure as a
771 function of strain, with failure occurring when ξ increased beyond 200 µm (Figure 13a). This limit
772 marks the longest crack supported by the sample volume without a runaway instability developing,
773 and falls just short of the mean grain size (i.e., the length between grain boundaries) of the
774 groundmass (250 µm – see Section 2.1). This implies that the sample breaks when whole grains
775 break. The nature of the increase in $\xi(\epsilon)$ in the untreated sample (blue) was exponential (i.e., had
776 the lowest $AICc$ – see Table S4 in SI) up to a finite ξ that fluctuated around 200 µm before failure.
777 Conversely, in the heat-treated sample (orange) $\xi(\epsilon)$ preferred a simple power-law acceleration
778 (Figure S4 and Table S4 in SI) to failure, failing when $\xi > 200$ µm. The exponent (6.9) is the same
779 (within error) as the exponents for the evolution of φ and N with strain (Section 3.2.1; Tables S2-
780 S4 in the SI), independently confirming that in this sample crack growth played an increasingly
781 important role closer to failure. The power-law acceleration emerges only once fractures began to
782 localize along the optimally oriented damage zone (at 90% σ_c and $\xi > \xi_0$), representing a strong
783 self-organization in the crack network over all distances to concentrate on the damage zone that
784 controls the eventual fault plane.

785   The two samples had different initial exponents β for their volume distributions (Figure
786 13b). In the untreated sample (blue) β rose sharply to a peak at the transition from the TRP to the
787 GR model. This shows that, at this point, the largest cracks in the taper were growing or opening,
788 while simultaneously many more small cracks were becoming active above the segmentation
789 detection threshold. The number of voids and the porosity were constant in this phase, implying
790 other voids were simultaneously closing in compaction (Figure 9b,c). This trade-off is consistent
791 with independent observations from acoustic emissions (Graham et al., 2010) and models (e.g.
792 Brantut et al., 2012; 2014) of the competition between compaction and dilatancy during the quasi-
793 elastic region of the stress-strain curve (Figure 9a). Beyond this peak, β decreased smoothly to the
794 first of two local minima once the additional radial zones had localized (Figure 4K). This indicates
795 instability in the sample-related crack nucleation (Figure 9c and Figure 10a) and might be
796 considered a precursor to failure, albeit without evidence of quasi-static damage zone propagation
797 within the temporal resolution of the method. Conversely, in the heat-treated sample (orange) β
798 decreased throughout, reflecting an increase in the relative proportion of larger micro-cracks. This
799 change occurred gradually at first and then more sharply once cracks localized along the optimally
800 oriented shear zone, similar to that observed in numerical simulations (Kun et al., 2013) and as
801 inferred from AE magnitude distributions (Sammonds et al., 1992) in dry porous media. The sharp
802 drop in β is a clear precursor to failure, corresponding to propagation of the shear zone through
803 the sample (Figure 5M-O). This supports our hypothesis that the heat-treated sample exhibits the
804 clear precursors associated with a second-order phase transition.

805   The evolution of the two-point correlation (fractal) dimension D was very different
806 between the two samples (Figure 13c). Initially there was a greater degree of clustering in the
807 untreated sample (blue) than the heat-treated one (orange). In both samples D shows a minimum
808 in the two time windows before the onset of localization, demonstrating the sensitivity of D to
809 localization (see also Bonnet et al., 2001). The degree of clustering at this point, reflected in the
810 value of D, was very similar between the two samples. From this point on, D in the untreated
811 sample increased significantly as micro-cracks became more distributed (less clustered) along the
812 radial zones. Conversely, in the heat-treated sample D shows increased clustering that was
813 sustained throughout localization. It recovered (implying decreased clustering) to a relatively

814   constant value as the optimally oriented shear zone propagated stably through the sample before
815   accelerating at the point of failure as the shear zone spanned the sample. Thus, D highlights clear
816   differences in the spatial distribution of the micro-crack network between the increasingly
817   distributed damage zones in the untreated sample and localization of an asymmetric shear fault in
818   the heat-treated one. The increasingly distributed nature of crack damage in the untreated sample
819   gives no indication of potential failure, while increased clustering due to localization in the heat-
820   treated sample is a clear and early precursor to failure associated with the development of a damage
821   zone optimally oriented to encourage system-sized shear failure. While both samples show
822   precursory changes, only the heat-treated sample has precursors capable of accurately forecasting
823   the point of system sized catastrophic failure.

824
825

Figure 13: Evolution with strain for (**a**) correlation length ξ, (**b**) microcrack volume exponent β, and (**c**) fractal dimension D, for the untreated (blue) and heat-treated (orange) samples. Error bars show (**b**) the standard error ($\beta/\sqrt{N}$) of the maximum likelihood estimate of β, where N is the number of cracks, and (**c**) the 95% confidence intervals of the linear regression fit for D. Dash-dot lines show the strain at which each sample failed, while dashed lines show the onset of localization as seen in the μCT volumes.

4 Discussion

The results presented above reveal key aspects of the evolving nature of compressive failure of brittle rocks through the accumulation of micro-cracks that spontaneously organize themselves along localized damage zones. Our synchrotron x-ray micro-tomography (μCT) observations of *in-situ* compressive rock deformation reveal the underlying processes – in particular the nature of the phase transition between intact and failed states in materials with different degrees of starting heterogeneity. Both our post-failure samples contained a localized shear fault, but the preceding accumulation of micro-cracks was very different between the samples, especially in their spatial distribution and their growth characteristics close to failure. We confirm our hypothesis that, in terms of stress and within the time-resolution of our experiments, the transition to failure is abrupt and unpredictable (first-order) in the homogeneous sample, but continuous and predictable (second-order) in the heterogeneous sample.

4.1   Microcrack network evolution

Prior to failure, our initially crack-free, and therefore more homogeneous, sample accumulated damage in a spalling pattern of localized zones distributed radially around the sample with no preferred strike direction. This damage pattern was completely overprinted during failure, highlighting the drawback of analyzing failed samples retrospectively to gain insights into pre-failure damage accumulation. Pre-failure behavior in this sample resembles strain localization observed from *in-situ* μCT images of deforming mono-minerallic, fine-grained and uniformly graded (i.e., structurally homogeneous) sand specimens (Desrues et al., 1996). The macroscopic fault localized abruptly at >97% of peak (failure) stress, σ_c, as microcracks transitioned from being broadly distributed throughout the sample (albeit along several radially oriented zones) to being organized along an emerging shear zone.

In contrast, our pre-cracked, and therefore more heterogeneous, sample accumulated damage around, and subsequently failed along, a localized shear zone. This behavior resembles the observations of Lockner et al. (1991; 1992) who showed progressive localization of AE along a shear zone in deforming Westerly granite samples from peak stress onwards. However, in our experiment the shear zone localized earlier, at 90% of σ_c, with a subsequent period of stable crack nucleation and growth along the damage zone during strain hardening prior to dynamic rupture at peak stress. This behavior resembles fault nucleation and propagation from AE in Berea (Lockner et al., 1992) and Clashach (Liakopoulou-Morris, et al. 1994; Lennart-Sassinek et al., 2014) sandstone samples (arguably more heterogeneous than granite samples in terms of their porosity), where a diffuse damage zone appeared and gradually localized around an incipient fault plane prior to σ_c.

Our results show that heterogeneity exerts a strong control on the evolution of crack network anisotropy, with homogeneity acting to stabilize the system prior to dynamic failure, generating more complex patterns of strain localization with more isotropic global characteristics, as suggested by Desrues et al., (1996). Under axi-symmetric triaxial loading conditions, sample homogeneity is a constraint that favors a transversely isotropic spalling pattern until very close to peak stress, whereas the presence of heterogeneity acts to amplify the pre-existing anisotropy with the formation of a shear fault. Radial spalling patterns are rarely observed in studies of AE, potentially due to limits on their location accuracy, where microcracks occurring along several radially distributed, but localized, damage zones might give the impression of being distributed throughout the sample.

877   In both of our samples, damage accumulated via the nucleation and sub-critical growth of
878   micro-cracks along localized damage zones. En-echelon and wing-crack arrays formed at different
879   stages in the deformation process in each sample (at initial localization in the untreated sample but
880   only once the optimally oriented shear zone localized in the heat-treated sample), and formed at
881   the same degree of strain (Figure 4F and Figure 5L), implying a degree of strain control. The main
882   direction of individual micro-crack growth in the localized zones was along strike rather than down
883   dip (Figure 10a,b,c). Models of damage accumulation under tri-axial compression are usually
884   based on AE locations and microstructural observations of post-failure samples, from which it is
885   difficult to quantify the relative proportion of progressive, pre-failure axial to radial micro-crack
886   growth. Along-strike growth is consistent with our conventional tri-axial compressional stress
887   configuration ($\sigma_1 > \sigma_2 = \sigma_3$), in which it is energetically more favorable for tensile micro-cracks
888   to open radially against the axes of minimum principal stress and close against the axis of
889   maximum principal stress. Down-dip fault propagation occurred instead by the nucleation, growth
890   and then linkage of an increasing number of small, tensile en-echelon and wing cracks forming at
891   the fault tip (Figure 6a,b, Figure 7 and Figure 9c). This is consistent with previous experimental
892   and modelling work (e.g., Tapponnier and Brace, 1976; Kranz, 1979; Nemat-Nasser and Horii,
893   1982; Horii and Nemat-Nasser, 1985; 1986; Sammis and Ashby, 1986; Ashby and Hallam, 1986;
894   Nemat-Nasser and Obata, 1988; Rundle and Klein, 1989; Ashby and Sammis, 1990; Reches and
895   Lockner, 1994; Potyondy and Cundall, 2004; Cho et al., 2007) and recent *in-situ* observations of
896   damage accumulation in strong rocks (Renard et al., 2017; 2018).

897   We observed significant anisotropy of void strike in the pre-existing porosity in both
898   samples (Figure 6c,d), despite visual inspection of thin sections and compressional wave velocities
899   of the same rock type showing only 1% anisotropy in bench-top tests on the original material
900   (Meredith et al., 2005; Meredith, pers comm.). This indicates that a small velocity anisotropy
901   represents substantial void anisotropy. The pre-existing void anisotropy is more pronounced in the
902   heat-treated sample than in the untreated sample, possibly due to thermal expansion during the
903   heat-treatment acting to close the isolated, mainly round voids in the feldspar micro-phenocrysts
904   (Meredith et al., 2012). This may also account for the otherwise counter-intuitive smaller overall
905   porosity in the heat-treated sample compared with the untreated one. The application of confining
906   pressure may also have contributed to the porosity difference by acting to close the thermally-
907   induced cracks in the heat-treated sample more effectively than the stiffer pores in the untreated
908   sample. In the heterogeneous sample, the preferred strike of the pre-existing porosity corresponds
909   almost exactly to the strike of the emerging fault plane (Figure 6d). There was also significant
910   amplification of the pre-existing anisotropy of the rock fabric (from 33% to 96% just before failure;
911   Table S1 in SI). This was not the case in the homogeneous sample, where the degree of anisotropy
912   remained approximately constant throughout the lead-up to failure (Table S1 in SI), consistent
913   with the lack of an overall preferred strike in the pre-failure localized zones in this sample.

914   The results in the previous paragraph prove that the initial microstructure, specifically the
915   orientation and anisotropy of pre-existing porosity dictated the geometry and location of the future
916   (post-failure) fault, particularly in the heat-treated sample. We speculate that this happens via a
917   modification of the local stress field with respect to the principal stress axes. In true tri-axial
918   configurations ($\sigma_1 > \sigma_2 > \sigma_3$), shear wave velocity anisotropy measurements have shown that
919   micro-cracks in general propagate parallel to σ_2 as they open parallel to σ_3 (Crawford et al., 1995),
920   while polymodal faulting is also often seen (Healy et al., 2015). Thus, although the global stress
921   configuration is axi-symmetric in our case, both heterogeneity and void anisotropy in the
922   microstructure appear to cause the local development of truly tri-axial stresses such that a particular

923 strike is preferred. One possible mechanism for this may be stress rotation around microstructural
924 discontinuities (Faulkner et al., 2006), possibly reflected in our experiments in the rotation of the
925 void ellipsoids with respect to the principal stress axes (Figure 6c,d). In this case, the pre-existing
926 network of anisotropic micro-cracks with a preferred orientation would have generated an
927 emergent, locally dominant true-triaxial stress field within the body of our heterogeneous sample,
928 even though the confining pressure was isotropic around the vertical (σ_1) axis. Conversely, in our
929 homogeneous sample, some complex interplay between local true tri-axial stresses and global axi-
930 symmetry would be required to generate several radially distributed damage zones simultaneously.
931 We speculate that the global axi-symmetry initially counteracts the rotation of internal stresses in
932 this sample, acting to prevent an increase in crack anisotropy and thereby increasing the uniformity
933 of the strike distribution as the experiment progresses. Thus, the relationship between the evolving
934 anisotropy of the micro-cracks and their preferred orientation is likely to be a controlling factor on
935 the geometry and location of an asymmetric shear fault, on the timing of the formation of this fault
936 and on whether pre-failure damage is localized along this fault or not.

937 In both our samples, the majority of cracks dip steeply within ±15° of the loading direction,
938 although a few dip less steeply between 15 and 30° (Figure 6a,b). This is consistent with the results
939 of post-failure sample analysis in early experimental work (Brace et al. 1966; Hallbauer et al. 1973;
940 Lajtai 1974). The macroscopic fault in our homogeneous sample dips at a similar angle to the pre-
941 failure micro-cracks, whereas in our heterogeneous sample it dips less steeply post-failure than it
942 does at peak stress. Although the effective pressure was relatively low (15 MPa), which may
943 promote axial failure over shear, it was consistent across the two experiments. This implies that
944 the differences in fault dip result from an intrinsic microstructural response, whereby the emergent
945 internal friction coefficient decreases during failure in the heterogeneous sample but remains
946 constant in the homogeneous sample, consistent with DEM models (Kun et al., 2018) that show a
947 decreasing coefficient of internal friction with increasing heterogeneity. In both samples, the dip
948 angle increases during quasi-static damage accumulation, increasing earlier in the homogeneous
949 case (during initial localization) than the heterogeneous case (only during localization around the
950 optimally oriented shear zone). In the homogeneous case, the steep dip of the nucleating cracks
951 (Figure 6a and Figure 7a) and the eventual fault plane (10°; Figure 6a) indicates that the internal
952 friction coefficient in this sample is sufficiently high to inhibit micro-crack damage by shear
953 mechanisms until immediately before dynamic failure. In the heterogeneous case, the dip, and
954 therefore the internal friction coefficient, increases only during propagation of the shear zone and
955 is particularly pronounced immediately before failure (Figure 6b), while the eventual fault plane
956 dips less steeply (30°; Figure 6b). This indicates that early crack nucleation and failure itself both
957 involve shear mechanisms, but shear zone propagation is governed primarily by tensile
958 mechanisms, i.e., the accumulation of en-echelon tensile cracks (Figure 7b), with a corresponding
959 increase in the internal friction coefficient. For this reason we have referred to a 'damage zone'
960 prior to failure and a 'fault plane' afterwards.

961 In our homogeneous sample, increased clustering (Figure 13c; blue circles) occurred at
962 43% σ_c with the onset of localization at 64%. This agrees with observations and models of cracks
963 initiating earlier than the theoretical shear-sliding threshold for more homogeneous low porosity,
964 crystalline rocks (70% σ_c; Hallbauer et al., 1973; Nicksiar and Martin, 2013; 2014). The
965 implication is that our more homogeneous sample is weakest in tension and, once a sufficient
966 number of tensile cracks form, a macroscopic shear fracture will naturally develop. We therefore
967 conclude that damage in this sample most likely initiated via the nucleation of pore-emanating
968 (Sammis and Ashby, 1986; Ashby and Sammis, 1990) or force-chain controlled (Potyondy and

969   Cundall, 2004; Cho et al., 2007) tensile micro-cracks due to the re-distribution of stress around
970   equant compressing pores and grains. Conversely, increased clustering in our heterogeneous
971   sample (Figure 13c; orange circles) occurred at 62% σ_c with the onset of localization at 72%. This
972   is later than the theoretical shear-sliding threshold for heterogeneous rocks (60% σ_c; Hallbauer et
973   al., 1973; Nicksiar and Martin, 2013; 2014). The implication here is that our more heterogeneous
974   sample is weaker in shear than in tension since shear sliding along preferentially oriented, pre-
975   existing cracks occurred before tensile cracking. We therefore conclude that damage in this sample
976   most likely initiated via the development of tensile 'wing-cracks' (Nemat-Nasser and Hori, 1982;
977   Horii and Nemat-Nasser, 1985; 1986; Ashby and Hallam, 1986; Nemat-Nasser and Obata, 1988;
978   Ashby and Sammis, 1990) at the tips of pre-existing defects due to shear-sliding along those
979   defects. Unfortunately, such shear sliding would not be visible in our images without significant
980   dilatancy during slip.

981   In summary, our experimental data confirm that the initial heterogeneity within a rock
982   sample is a key control over how cracks, pores and grain boundaries interact locally with the
983   applied stress field, and imply that the microstructure transitions from being weakest in tension to
984   being weakest in shear as heterogeneity increases.

985   **4.2   Scaling, phase transition style and predictability of failure time**

986   Micro-crack volume and inter-crack length distributions follow power-laws throughout the
987   cycle of deformation and failure in both samples, characteristic of the scale-invariant (fractal)
988   nature of natural fault networks (Main et al., 1990; Bonnet et al., 2001) and consistent with the
989   power-law microcrack volume distributions observed by Renard et al. (2017; 2018). The transition
990   from the TRP to the GR model for the micro-crack volume distributions (Figure S2 in SI) in the
991   homogeneous sample emulates changes in the organization of earthquake size distributions
992   following the occurrence of extreme or very large earthquakes (Bell et al., 2013a). Close to failure
993   the void volume distribution shows a bump at large volumes, indicative of a supercritical state
994   with an elevated probability of occurrence of large events (Main, 1996), sometimes known as
995   'dragon kings' (Sornette, 2009). We have demonstrated that the parameters of these distributions
996   are more sensitive to heterogeneity than porosity alone, consistent with the findings of Vasseur et
997   al. (2017) and Kun et al. (2018). In combination with μCT observations of fault formation, the
998   evolution of these parameters provides a microstructural explanation for the variation in the
999   systematic prediction error for the failure time based on acoustic emissions (Vasseur et al. 2015).

1000   However, the systematic change in the mean void aspect ratios during crack growth may
1001   indicate that the scaling of crack growth is self-affine (i.e., exhibits scale-invariance in length with
1002   different exponents for individual growth axes, leading to a variable aspect ratio) rather than self-
1003   similar (the same scaling exponent for all growth axes, with a constant aspect ratio). This is
1004   consistent with observations of fracture surface geometries in rocks (Schmittbuhl et al., 1995) and
1005   other materials (Mandlebrot et al., 1984; Bouchaud et al., 1990; Russ, 1994; Schmittbuhl and
1006   Maloy, 1997; see also Bouchaud, 1997 for a review), which are well-described by self-affine
1007   fractals. These studies have shown that scaling along the aperture axis is systematically smaller
1008   than along the mean crack plane, with the systematic (Hurst) exponent defining the fracture
1009   roughness (Bouchaud, 1997; Weiss, 2001). Our observation that almost no growth at all occurs
1010   along the aperture axis supports the conjecture that the aperture direction is not physically
1011   equivalent to the mean crack plane (Schmittbuhl et al., 1995). Our results indicate that scaling
1012   along the strike and dip axes may also systematically differ from each other. This contradicts the

1013   notion of strict self-similarity in the mean crack plane (Schmittbuhl et al., 1995), and implies that
1014   the strike and dip directions are not physically equivalent either. Further work is required to
1015   quantify the scaling anisotropy for crack growth in our experiments and to test these hypotheses.
1016   Since crack surfaces in crystalline materials require heterogeneities, such as grain boundaries and
1017   dislocations that pin the propagating crack front, in order to develop self-affine roughness
1018   (Schmittbuhl and Maloy, 1997; Bouchaud, 1997; Weiss, 2001), we expect that scaling exponents
1019   for the heterogeneous sample may be more anisotropic than for the homogeneous sample.

1020   In the heterogeneous (heat-treated) case, we find evidence for a continuous (second-order)
1021   phase transition in the inverse power-law acceleration to failure of ξ with respect to stress (Figure
1022   12; solid orange line), with failure occurring near the asymptote, together with clear precursors in
1023 β and D. The rapid decrease in β corresponds to the formation of a localized damage zone
1024   optimally oriented for macroscopic shear failure, occurring when the microcrack network self-
1025   organizes. This provides a clear precursor to sample failure related to a distinct physical process,
1026   i.e. the emergent inverse power-law acceleration in ξ. The asymptote defines a predictable failure
1027   time defined by a smooth transition to an infinite ξ at the sample-scale (Figure 1; orange line). The
1028   early and sustained decrease in D in 3D is a key precursory indicator of localization, while its
1029   recovery is associated with shear zone propagation in 2D, as anticipated by the model of Main
1030   (1992). This provides another clear precursor to failure. Such behavior agrees with statistical
1031   physics models of rupture as a critical, second-order phenomenon (Girard et al., 2010; Kun et al.,
1032   2013). Thus, taken together, these variables show that damage localization along a zone optimally
1033   orientated for macroscopic shear failure is the physical process that defines whether the phase
1034   transition from an intact to a failed state is second-order, and therefore predictable, with reliable
1035   precursors to failure.

1036   In the homogeneous (untreated) case, we find evidence for an abrupt or discontinuous
1037   (first-order) phase transition, with an unsuccessful forecast of the failure stress, and a preference
1038   for an exponential model for the evolution of the correlation length, ξ, with respect to stress.
1039   Furthermore, there is very little evidence for reliable precursors in either the micro-crack volume
1040   exponent, β, or the two-point fractal dimension, D, and the bump in the void size distribution at
1041   large volumes is reminiscent of a first-order phase transition (Lominitz-Adler et al., 1992; Ceva
1042   and Perazzo, 1993). Approaching failure we see small fluctuations in β, ξ and D that may indicate
1043   impending failure as they are associated with formation of the additional damage zones and
1044   subsequent microstructural instability due to crack nucleation close to failure. However, using
1045   these parameters as precursors may lead to false alarms since they are not associated with the
1046   eventual fault plane. The exponential increase in ξ (implying that local correlations dominate) is
1047   unusual and generally associated with the critical regime during phase transitions across surfaces
1048   (Kosterlitz and Thouless, 1973; Kosterlitz, 1974), such as during large-scale faceting at the
1049   surfaces of growing crystals (Nozières, 1992). Its stabilization to a finite value shortly followed by
1050   abrupt failure is characteristic of a first order phase transition (Figure 1; green line). In numerical
1051   models of fault growth, an exponential distribution of fault lengths is associated with crack
1052   nucleation, whereas a power-law distribution emerges with nucleation plus crack growth and
1053   coalescence (Cowie et al., 1995). Hence, the origin of this response in our rock volume may be
1054   explained by our observation that crack nucleation is the dominant damage process in the
1055   homogeneous sample while crack growth becomes increasingly important closer to failure in the
1056   heterogeneous sample (Section 3.2.1). This behavior corresponds to the existence of a metastable
1057   state of crack nucleation at a system-sized ξ during a first-order transition, when the system is

1058 vulnerable to the influence of sufficiently large perturbations (subcritical bifurcation) (Sornette,
1059 2006). This vulnerability and the resulting discontinuity may be the reason for an unpredictable
1060 failure time (Vasseur et al., 2015).

1061 An estimate for the correlation length exponent (1.15) for Carrara marble (Kandula et al.,
1062 2019) falls almost exactly halfway between the exponents for Ailsa Craig microgranite found here
1063 (0.65 for the heterogeneous sample and 1.75 for the homogeneous sample). However, the Carrara
1064 marble exponent was estimated by assuming the failure stress *a priori*, so it is not directly
1065 comparable with our results. It is therefore not possible to confirm whether an inverse power-law
1066 would successfully forecast the failure stress in real time and/or whether a different model would
1067 be more likely. Nevertheless, the nature of Carrara marble may place it halfway between our two
1068 end members. It is chemically pure, composed of 99% annealed calcite crystals (Alber and
1069 Hauptfleisch, 1999), with a homogeneous microstructure (Oesterling, 2004), a very low
1070 permeability (10^{-19} m^2) and only 0.2-0.5% connected porosity (Zhang, 1994; Alber and
1071 Hauptfleisch, 1999; Bandini et al., 2012; Cartwright-Taylor et al., 2015). However, studies have
1072 shown the presence of micro-discontinuities within grains, including twin lamellae (Ramez and
1073 Murrell, 1964; Bandini et al., 2012; Cartwright-Taylor et al., 2015) and a high density of
1074 dislocations (Fredrich et al., 1989), while its isotropic texture consists of both well-locked
1075 (xenoblastic) and more mobile (granoblastic) grain boundaries (Bandini et al., 2012; Cartwright-
1076 Taylor et al., 2015). These factors indicate a complex history of both static and dynamic
1077 recrystallization (Molli and Heilbronner, 1999; Oesterling, 2004) and introduce a degree of
1078 heterogeneity that may be intermediate between our two samples.

1079 In both samples, the critical value of ξ is 200 μm, marking the longest crack supported by
1080 the sample volume without a runaway instability developing. Significantly, this falls just short of
1081 the mean grain size of the groundmass (250 μm). That is, catastrophic failure occurs when whole
1082 grains break. This confirms the findings of Vasseur et al. (2017) from acoustic emissions (AE)
1083 data that the grain size (inter-particle distance) is a better metric for the characteristic void
1084 dimension at failure than the distance between pores (inter-void distance).

1085 Our observations highlight the strong dependence of the degree of predictability on
1086 material properties that may be unknown in a field application, as well as the importance of
1087 analyzing several independent parameters for identifying the type of phase transition and
1088 predicting the point of failure (Lei and Satoh, 2007). They may also explain why, when looking at
1089 long time-series of field-scale seismicity or deformation, clear and reliable precursors to failure
1090 are detected only in some cases, and preferentially in application to forecasting of landslides and
1091 volcanic eruptions. In other cases, notably in forecasting of individual large earthquakes,
1092 fluctuations related to instability may be present but may not be statistically significant enough to
1093 be detectable as precursors. In both samples, *D* shows increased clustering earlier than localization
1094 is visually apparent in the μCT images, and therefore may provide useful information about the
1095 impending onset of damage localization for a variety of applications and settings. Finally, the
1096 relatively high strain rates analyzed here may not be representative of the evolution of precursors
1097 at lower strain rates. For example Ojala et al. (2004) showed that the acceleration to failure in AE
1098 rate asymptotically approaches the behaviour expected of a single Griffith crack (Figure 1) as
1099 strain rate is decreased in laboratory compression tests on porous sandstones. Nevertheless, we
1100 have confirmed that heterogeneity plays a significant role in determining the style of evolution of
1101 the population of micro-cracks, and hence the predictability of the system-scale failure time.

4.3   Suggestions for future work

This discussion has highlighted some outstanding research questions to be addressed in future work. The most notable of these are as follows: (i) Why do previously obtained degrees of anisotropy inferred from acoustic measurement differ markedly from our newly obtained structural ones? (ii) How does crack growth scale (in terms of the ellipsoid radii), and is it self-affine? (iii) Does the predominant local failure mechanism change from tensile to shear as system-sized failure approaches, as seen in the AE data of Graham et al. (2010)? (iv) Does this transition occur earlier in more heterogeneous materials? Given tensile fractures are easier to see in imaging void space, the latter two questions would benefit from digital volume correlation techniques that are the subject of ongoing work, and can detect local changes in shear and volumetric strain.

5 Conclusions

Our *in-situ* time-resolved x-ray μCT images of very small samples of deforming granite show that the heterogeneity of the starting material exerts a strong control on the evolution of the statistical properties of crack size and spatial distribution during fracture network evolution. The accumulating micro-cracks have power-law frequency-volume and inter-crack length distributions over a finite scaling range, irrespective of the degree of starting heterogeneity, with well-determined scaling exponents β (the size exponent) and D (the correlation dimension). The inferred correlation length ξ increases exponentially with respect to stress in the homogeneous case, with sudden-onset, unpredictable failure, analogous to the behavior expected for a first-order (discontinuous) phase transition. In contrast, the heterogeneous sample shows an inverse power-law acceleration to a predictable failure point at the asymptote, diagnostic of a second-order (continuous) phase transition (Equation 1 and Figure 1). The second-order transition is linked to the distinct physical process of quasi-static, asymmetric accumulation of damage within an optimally-oriented zone increasingly localized around the eventual fault plane, with associated reliable precursors to failure in the evolution of β and D. The correlation dimension is a key early indicator of localization on such a shear zone for the heterogeneous sample. This is not observed within the time resolution of our observations for the homogeneous sample, where the precursory damage takes the form of more radially isotropic zones of spalling, and shear localization must occur very close to the point of dynamic failure itself to explain the post-failure observation of a shear fault.

Crack nucleation dominates the frequency-size statistics in the homogeneous case and crack growth in the heterogeneous case. In both cases, the transition to localized damage occurs by a combination of nucleation and growth. The timing of the onset of crack coalescence defines the order of the phase transition, and hence the predictability of the failure time. Nevertheless, catastrophic failure occurs in both cases as the correlation length approaches the grain size, which in turn controls the failure of local bridges between aligned en-echelon and wing-cracks in the shear damage zone in the heterogeneous sample. The initial rock microstructure, specifically the anisotropy of pre-existing porosity, dictates the geometry and orientation of the emergent fault plane, independent of starting heterogeneity. This reflects the strong control of starting microstructure on the rock's internal stress state, despite the axi-symmetric external loading conditions and the very low anisotropy (1%) inferred from acoustic velocity measurement.

Appendix A. Supporting Information (SI)

Supporting information related to this article can be found in the accompanying document.

References

Abercrombie, R.E. (1995), Earthquake source scaling relationships from -1 to 5 ML using seismograms recorded at 2.5-km depth, J. Geophys. Res. 100, 24015–24036.

Aki, K. (1965), Maximum likelihood estimate of b in the formula $\log N = a - bM$ and its confidence limits, Bull. Earthquake Res. Inst. 43, 237-239.

Alava, M.J., Nukala, P.K.V. and Zapperi, S. (2008), Fracture size effects from disordered lattice models, Int. J. Fract. 154, 51-59.

Alber, M. and Hauptfleisch, U. (1999), Generation and visualization of micro-fractures in Carrara marble for estimating fracture toughness, fracture shear and fracture normal stiffness, Int. J. Rock Mech. Min. Sci. 36, 1065-1071.

Andrew, M. (2018), A quantified study of segmentation techniques on synthetic geological XRM and FIB-SEM images, Computational Geosciences 22, 1503-1512.

Ashby M.F. and Sammis, C.G. (1990), The damage mechanics of brittle solids in compression, PAGEOPH 133, 489-521.

Ashby, M.F. and Hallam, S.D. (1986), The failure of brittle solids containing small cracks under compressive stress states, Acta Metall. 34, 497-510.

Bandini, A., Berry, P., Bemporad, E., and Sebastiani, M. (2012), Effects of intra-crystalline microcracks on the mechanical behavior of a marble under indentation, Int. J. Rock Mech. Min. Sci. 54, 47-55.

Bell, A.F., Naylor, M. and Main, I.G. (2013a), Convergence of the frequency-size distribution of global earthquakes, Geophys. Res. Lett. 40, 2585-2589.

Bell, A.F., Naylor, M. and Main, I.G. (2013b), The limits of predictability of volcanic eruptions from accelerating rates of earthquakes, Geophys. J. Int. 194, 1541-1553.

1181 Bonnet, E., Bour, O., Odling, N.E., Davy, P., Main, I., Cowie, P. and Berkowitz, B. (2001), Scaling
1182   of fracture systems in geological media, Rev. Geophys. 39, 347-383.

1183 Bouchaud, E. (1997), Scaling properties of cracks, J. Phys. Condens. Matter 9, 4319-4344.

1184 Bouchaud, E., Lapasset, G., and Planès, J. (1990), Fractal dimension of fractured surfaces: a
1185   universal value?, Europhys. Lett. 13, 73-79.

1186 Brace, W.F., Paulding, B. and Scholz, C. (1966), Dilatancy in the fracture of crystalline rocks. J.
1187   Geophys. Res. 71, 3939-3953.

1188 Brantut, N., Baud, P., Heap, M.J. and Meredith, P.G. (2012), Micromechanics of brittle creep in
1189   rocks, J. Geophys. Res. 117, B08412.

1190 Brantut, N., Heap, M.J., Baud, P. and Meredith, P.G. (2014), Rate- and strain-dependent brittle
1191   deformation of rocks, J. Geophys. Res. Solid Earth 119, 1818-1836.

1192 Bruce, A. and D. Wallace (1989). Critical point phenomena: universal physics at large length
1193   scales, in: Davies, P. (ed.), The New Physics, Cambridge University Press, Cambridge UK.

1194 Bruner, W.M. (1984), Crack growth during unroofing of crustal rocks: effects of thermoelastic
1195   behavior and near-surface stresses, J. Geophys. Res. 89, 4167-4184.

1196 Bruner, W.M. (1979), Crack growth and the thermoelastic behavior of rocks, J. Geophys. Res. 84,
1197   5578-5590.

1198 Bufe, C.G. and Varnes, D.J. (1993), Predictive modeling of the seismic cycle of the greater San
1199   Francisco Bay region, J. Geophys. Res. 98, 9871-9883.

1200 Burnham, K.P. and Anderson, D.R. (2002), Model selection and multi-model inference: a practical
1201   information-theoretic approach (2nd ed.), Springer, New York.

1202 Butler, I.B., Flynn, M., Fusseis, F. and Cartwright-Taylor, A. (2017), Mjolnir: a novel x-ray
1203   transparent triaxial rock deformation apparatus, ICTMS2017-56, 3rd International
1204   Conference on Tomography of Materials and Structures, Lund, Sweden, 26-30 June.

1205 Cartwright-Taylor, A. (2015), Deformation-induced electric currents in marble under simulated
1206   crustal conditions: non-extensivity, superstatistical dynamics and implications for
1207   earthquake hazard, PhD thesis, University College London.

1208 Cartwright-Taylor, A., Main, I.G., Butler, I.B., Fusseis, F., Flynn M. and King, A. (2020): In-situ
1209   rock deformation and micron-scale crack network evolution: a high-resolution time-
1210   resolved x-ray micro-tomography dataset, British Geological Survey (Dataset)
1211   https://doi.org/10.5285/0dc00069-8da8-474a-8993-b63ef5c25fb8.

1212 Ceva, H. and Perazzo, R.P.J. (1993), From self-organized criticality to first-order-like behaviour:
1213   A new type of percolative transition, Phys. Rev. E 48, 157-160.

1214 Cho, N., Martin, C.D. and Sego, D.S. (2007), A clumped particle model for rock, Int. J. Rock
1215   Mech. Min. Sci. 44, 997-1010.

1216 Clint, O.C., Meredith, P.G. and Main, I.G. (2001), Relation between crack damage and
1217   permeability near the percolation threshold in a near perfect crystalline rock, Geophys. Res.
1218   Abstr. 3, 346.

1219 Cornelius, R.R. and Voight, B. (1994), Seismological aspects of the 1989-1990 eruption at
1220   Redoubt Volcano, Alaska: The Materials Failure Forecast Method (FFM) with RSAM and
1221   SSAM seismic data, J. Volcanol. Geotherm. Res. 62, 469-498.

1222 Cowie, P.A., Sornette, D. and Vanneste, C. (1995), Multifractal scaling properties of a growing
1223   fault population, Geophys. J. Int. 122, 457-469.

1224 Crawford, B.R., Smart, B.G.D., Main, I.G. and Liakopoulou-Morris, F. (1995). Strength
1225   characteristics and shear acoustic anisotropy of rock core subjected to true triaxial
1226   compression, Int. J. Rock Mech. Min. Sci. 32, 189-200.

1227 Damjanac, B. and Fairhurst, C. (2010), Evidence for a long-term strength threshold in crystalline
1228   rock, Rock Mech. Rock Eng. 43, 513-531.

1229 David, C., Menendez, B. and Darot, M. (1999), Influence of stress-induced and thermal cracking
1230   on physical properties and microstructure of La Peyratte granite, Int. J. Rock Mech. Min.
1231   Sci. 36, 433–448.

1232 Descoteaux, M., Audette, M., Chinzei, K. and Siddiqi,K. (2005), Bone enhancement filtering:
1233   application to sinus bone segmentation and simulation of pituitary surgery, in: Duncan, J.S.
1234   and Gerig, G. (eds.), Proceedings of Medical Image Computing and Computer-Assisted
1235   Intervention (MICCAI), Palm Springs, California, USA, Lecture Notes in Computer
1236   Science 3749, 09–16.

1237 Desrues, J., Chambon, R., Mokni, M. and Mazerolle, F. (1996), Void ratio evolution inside shear
1238   bands in triaxial sand specimens studied by computed tomography, Geotechnique 46, 529-
1239   546.

1240 Fairhurst, C. and Cook, N.G.W. (1966), The phenomenon of rock splitting parallel to the direction
1241   of maximum compression in the neighborhood of a surface, In: Zeitlen, J.G. (ed)
1242   Proceedings of First Congress of the International Society of Rock Mechanics (Lisbon,
1243   September-October 1966) Vol 1., LNEC, Lisbon, 687-692.

1244 Faulkner, D.R., Mitchell, T.M., Healy, D. and Heap, M.J. (2006), Slip on 'weak' faults by the
1245   rotation of regional stress in the damage zone, Nature 444, 922-925.

1246 Fredrich, J.T., and Wong T.-F. (1986), Micromechanics of thermally induced cracking in three
1247   crustal rocks, J. Geophys. Res. 91, 12743–12764.

1248 Fredrich, J.T., Evans, B., and Wong, T.-F. (1989), Micromechanics of the brittle to plastic
1249   transition in Carrara marble. J. Geophys. Res. Solid Earth 94, 4129-4145.

1250 Fusseis, F., Steeb, H., Xiao, X., Zhu, W., Butler, I., Elphick, S. and Mäder, U. (2014), A low-cost
1251   X-ray-transparent experimental cell for synchrotron-based X-ray microtomography studies
1252   under geological reservoir conditions, J. Synchrotron Rad. 21, 251-253.

1253 Girard, L., Amitrano, D. and Weiss, J. (2010), Failure as a critical phenomenon in a progressive
1254   damage model, J. Stat. Mech. Theory Exp. P01013.

1255 Goodfellow, S.D. and Young, R.P. (2014), A laboratory acoustic emission experiment under in-
1256   situ conditions, Geophys. Res. Lett. 41, 3422-3430.

1257 Graham, C.C., Stanchits, S., Main, I.G. and Dresen, G. (2010), Comparison of polarity and
1258   moment tensor inversion methods for source analysis of acoustic emission data, Int. J. Rock
1259   Mech. Min. Sci. 47, 161-169.

1260 Greenhough, J. and Main, I.G. (2008), A Poisson model for earthquake frequency uncertainties in
1261   seismic hazard analysis, Geophys. Res. Lett. 35, L19313.

1262 Griffith, A.A. (1921), The phenomena of rupture and flow in solids, Phil. Trans. R. Soc. A 221,
1263   163-198.

1264 Griffith, A.A. (1924), Theory of rupture, Proc. First Int. Congress Appl. Mech., Delft, 55-63.

1265 Griffiths, L., Lengliné, O., Heap, M.J., Baud, P. and Schmittbuhl, J. (2018), Thermal cracking in
1266   Westerly granite monitored using direct wave velocity, coda wave interferometry and
1267   acoustic emissions, J, Geophys. Res. Solid Earth 123, 2246-2261.

1268 Guéguen, Y. and Schubnel, A. (2003), Elastic wave velocities and permeability of cracked rocks,
1269   Tectonophys. 370, 163-176.

1270 Hallbauer, D.K., Wagner, H. and Cook N.G.W. (1973), Some observations concerning the
1271   microscopic and mechanical behaviour of quartzite specimens in stiff, triaxial compression
1272   tests, Int. J. Rock Mech. Min. Sci. Geomech. Abstr. 10, 713-726.

1273 Haneberg, W.C. (2004), Computational Geosciences with Mathematica, Springer-Verlag, Berlin
1274   Heidelberg New York.

1275 Healy, D., Blenkinsop, T.G., Timms, N.E., Meredith, P.G., Mitchell, T.M. and Cooke, M.L.
1276   (2015), Polymodal faulting: time for a new angle on shear failure, J. Struct. Geol. 80, 57-
1277   71.

1278 Hildebrand, T. and Rüegsegger, P. (1997), A new method for the model-independent assessment
1279   of thickness in three-dimensional images, J. Microscopy 185, 67-75.

1280 Horii, H. and Nemat-Nasser, S. (1985), Compression-induced microcrack growth in brittle solids:
1281   axial splitting and shear failure, J. Geophys. Res. 90, 3105-3125.

1282 Horii, H. and Nemat-Nasser, S. (1986), Brittle failure in compression: splitting, faulting and brittle-
1283   ductile transition, Phil. Trans. R. Soc. A 319, 337-374.

1284 Hurvich, C.M. and Tsai, C.-L. (1989), Regression and time series model selection in small
1285   samples, Biometrika 76, 297-307.

1286 Kagan, Y.Y. (2002), Seismic moment distribution revisited: i. statistical results, Geophys. J. Int.
1287   148, 520-541.

1288 Kagan, Y.Y. and Schoenberg, F. (2001), Estimation of the upper cutoff parameter for the tapered
1289   Pareto distribution, J. Appl. Probab. 38, 168-185.

1290 Kamb, W.B. (1959), Ice petrofabric observations from Blue Glacier, Washington, in relation to
1291   theory and experiment, J. Geophys. Res. 64, 1891-1909.

1292 Kandula, N., Cordonnier, B., Boller, E., Weiss, J., Dysthe, D.K. and Renard, F. (2019), Dynamics
1293   of microscale precursors during brittle compressive failure in Carrara marble, J. Geophys.
1294   Res. Solid Earth, 124, 6121-6139.

1295 Kijko, A. and Graham, G. (1998), Parametric-historic procedure for probabilistic seismic hazard
1296   analysis part i: estimation of maximum regional magnitude m_{max}, PAGEOPH 152, 413-
1297   442.

1298 Kilburn, C.R.J. (2003), Multiscale fracturing as a key to forecasting volcanic eruptions, J.
1299   Volcanol. Geotherm. Res. 125, 271-289.

1300 Kilburn, C.R.J. and Voight, B. (1998), Slow rock fracture as eruption precursor at Soufriere Hills,
1301   Geophys. Res. Lett. 25, 3665-3668.

1302 Kosterlitz, J.M. (1974), The critical properties of the two-dimensional xy model, J. Phys. C: Solid
1303   State Phys. 7, 1046-1060.

1304 Kosterlitz, J.M. and Thouless, D.J. (1973), Ordering, metastability and phase transitions in two-
1305   dimensional systems, J. Phys. C: Solid State Phys. 6, 1181-1203.

1306 Kranz, R.L. (1979), Crack-crack and crack-pore interactions in stressed granite, Int. J. Rock Mech.
1307   Min. Sci. Geomech. Abstr. 16, 37-47.

1308 Kun, F., Pal, G., Varga, I. and Main, I.G. (2018), Effect of disorder on the spatial structure of
1309   damage in slowly compressed porous rocks, Phil. Trans. R. Soc. A 377, 20170393.

1310 Kun, F., Varga, I., Lennartz-Sassinek, S. and Main, I.G. (2013), Approach to failure in porous
1311   granular materials under compression, Phys. Rev. E 88, 062207.

1312 Lajtai, E.Z. (1974), Brittle fracture in compression. Int. J. Fract. 10, 525-536.

1313 Lei, X. and Satoh, T. (2007), Indicators of critical point behavior prior to rock failure inferred from
1314   pre-failure damage, Tectonophys. 431, 97-111.

1315 Lei, X., Kusunose, K., Nishizawa, O., Cho, A. and Satoh, T. (2000), On the spatiotemporal
1316   distribution of acoustic emissions in two granitic rocks under triaxial compression: the role
1317   of pre-existing cracks, Geophys. Res. Lett. 27, 1997-2000.

1318 Lennartz-Sassinek, S., Main, I.G., Zaiser, M. and Graham, C.C. (2014), Acceleration and
1319   localization of subcritical crack growth in a natural composite material, Phys. Rev. E 90,
1320   052401.

1321 Leonard, T. and Hsu, J.S.J. (1999), Bayesian Methods, Cambridge University Press, Cambridge
1322   UK.

1323 Liakopoulou-Morris, F., Main, I.G., Crawford, B.R. and Smart, B.G.D. (1994), Microseismic
1324   properties of a homogeneous sandstone during fault nucleation and frictional sliding,
1325   Geophys. J. Int. 119, 219-230.

1326 Lockner, D., Byerlee, J.D., Kuksenko, V., Ponomarev, A. and Sidorin, A. (1992), Observations of
1327   quasi-static fault growth from acoustic emissions, in: Evans, B. and Wong, T.-F. (eds.),
1328   Fault Mechanics and Transport Properties of Rocks (1st ed.), International Geophysics 51,
1329   3-31.

1330 Lockner, D., Byerlee, J.D., Kuksenko, V., Ponomarev, A. and Sidorin, A. (1991), Quasi-static fault
1331   growth and shear fracture energy in granite. Nature 350, 39-42.

1332 Lominitz-Adler, J., Knopoff, L. and Martinez-Mekler, G. (1992), Avalanches and epidemic
1333   models of fracturing in earthquakes, Phys. Rev. A 45, 2211-2221.

Main, I.G. (1996), Statistical physics, seismogenesis and seismic hazard, Rev. Geophys. 34, 433-462.

Main, I.G., Meredith, P.G., Sammonds, P.R. and Jones, C. (1990), Influence of fractal flaw distributions on rock deformation in the brittle field, in: Knipe, R.J. and Rutter, E.H. (eds.), Deformation Mechanisms, Rheology and Tectonics, Geol. Soc. Spec. Pub. 54, 81-96.

Main, I.G. (1992). Damage mechanics with long-range interactions: correlation between the seismic b-value and the two point correlation dimension, Geophys. J. Int. 111, 531-541.

Main, I.G., Sammonds, P.R. and Meredith, P.G. (1993), Application of a modified Griffith criterion to the evolution of fractal damage during compressional rock failure, Geophys. J. Int. 115, 367-380.

Mandelbrot, B., Passoja, D.E., and Paullay, A.J. (1984), Fractal character of fracture surfaces of metals, Nature 308, 721-722.

Meijering, E.H.W. (2010), FeatureJ 1.6.0, Biomedical Imaging Group Rotterdam, Erasmus MC, University Medical Center Rotterdam, The Netherlands, 2002-2010 (http://www.imagescience.org/meijering/software/featurej/).

Meredith, P.G., Clint, O.C., Ngwenya, B., Main, I.G., Odling, N.W.A. and Elphick, S.C., (2005), Crack damage and permeability evolution near the percolation threshold in a near-perfect crystalline rock, in: Shaw, R.P., (ed.) Understanding the Micro to Macro Behavior of Rock-Fluid Systems, Geol. Soc. Spec. Pub. 249, 159-160.

Meredith, P.G., Main, I.G., Clint, O.C. and Li, L. (2012), On the threshold of flow in a tight natural rock, Geophys. Res. Lett. 39, L04307.

Mignan, A. and Woessner, J. (2012), Estimating the magnitude of completeness for earthquake catalogues. Community Online Resource for Statistical Seismicity Analysis, pp. 1–45.

Mirone, A., Brun, E., Gouillart, E., Tafforeau, P. and Kieffer, J. (2014), The PyHST2 hybrid distributed code for high speed tomographic reconstruction with iterative re-construction and a priori knowledge capabilities. Nucl. Instrum. Methods Phys. Res., Sect. B, Beam Interact. Mater. Atoms 324, 41–48.

Mitchell, T.M. and Faulkner, D.R. (2012), Towards quantifying the matrix permeability of fault damage zones in low porosity rocks, Earth Planet. Sci. Lett. 339-340, 24-31.

Molli, G. and Heilbronner, R. (1999), Microstructures associated with static and dynamic recrystallization of Carrara marble (Alpi Apuane, NW Tuscany, Italy), Geologie en Mijnbouw 78, 119-126.

Moura, A., Lei, X.-L., Nishizawa, O., 2005. Prediction scheme for the catastrophic failure of highly loaded brittle materials or rocks. J. Mech. Phys. Solids 53, 2435–2455

Nemat-Nasser, S. and Horii, H. (1982), Compression-induced nonplanar crack extension with application to splitting, exfoliation, and rockburst, J. Geophys. Res. 87, 6805-6821.

Nemat-Nasser, S. and Obata, M. (1988), A microcrack model of dilatancy in brittle materials, J. Appl. Mech. 55, 24-35.

Nicksiar, M. and Martin, C.D. (2013), Crack initiation stress in low porosity crystalline and sedimentary rocks, Eng. Geol. 154, 64-76.

1374 Nicksiar, M. and Martin, C.D. (2014), Factors affecting crack initiation in low porosity crystalline
1375   rocks, Rock Mech. Rock Eng. 47, 1165-1181.

1376 Nozieres, P. (1992), Shape and growth of crystals, in: Godrèche, C. (ed.), Solids Far From
1377   Equilibrium, Cambridge University Press, Cambridge UK.

1378 Odling, N.W.A., Elphick, S.C., Meredith, P., Main, I. and Ngwenya, B.T. (2007), Laboratory
1379   measurement of hydrodynamic saline dispersion within a micro-fracture network induced
1380   in granite, Earth Planet. Sci. Lett. 260, 407-418.

1381 Oesterling, N. (2004), Dynamic recrystallization and deformation mechanisms of naturally
1382   deformed Carrara marble: a study on one- and two-phase carbonate rocks, PhD thesis,
1383   University of Basel.

1384 Ojala I.O., Main, I.G. and Ngwenya, B.T. (2004), Strain rate and temperature dependence of
1385   Omori law scaling constants of AE data: implications for earthquake foreshock-aftershock
1386   sequences, Geophys. Res. Lett. 31, L24617.

1387 Ollion, J., Cochennec, J., Loll, F., Escudé C. and Boudier, T. (2013), TANGO: A Generic Tool for
1388   High-throughput 3D Image Analysis for Studying Nuclear Organization, Bioinformatics
1389   29, 1840-1841.

1390 Olson, J.E., & Pollard, D.D. (1991), The initiation and growth of en échelon veins, J. Struct. Geol.
1391   13, 595-608.

1392 Ouillon, G. and Sornette, D. (2000), The concept of 'critical earthquakes' applied to main
1393   rockbursts with time-to-failure analysis, Geophys. J. Int. 143, 454–468.

1394 Pál, G., Jánosi, Z., Kun, F. and Main, I.G. (2016). Fragmentation by slow compression of porous
1395   rocks, Physical Review E 94, 053003.

1396 Pisarenko, V.F. (1991), Statistical evaluation of maximum possible earthquakes, Phys. Solid Earth
1397   27, 757-763.

1398 Potyondy, D.O. and Cundall, P.A. (2004), A bonded particle model for rock, Int. J. Rock Mech.
1399   Min. Sci. 41, 1329-1364.

1400 Ramez, M.R.H. and Murrell, S.A.F. (1964), A petro-fabric analysis of Carrara marble. Int. J. Rock
1401   Mech. Min. Sci. Geomech. Abstr. 1, 217-229.

1402 Reches, Z. and Lockner, D.A. (1994), Nucleation and growth of faults in brittle rocks, J. Geophys.
1403   Res. 99, 18159-18173.

1404 Renard, F., Cordonnier, B., Dysthe, D.K., Boller, E., Tafforeau, P. and Rack A. (2016), A
1405   deformation rig for synchrotron microtomography studies of geomaterials under conditions
1406   down to 10 km depth in the Earth, J. Synchrotron Rad. 23, 1030-1034.

1407 Renard, F., Cordonnier, B., Kobchenko, M. and Kandula, N. (2017), Microscale characterization
1408   of rupture nucleation unravels precursors to faulting in rocks, Earth Plan. Sci. Lett. 476,
1409   69-78.

1410 Renard, F., Weiss, J., Mathiesen, J. Ben-Zion, Y., Kandula, N. and Cordonnier, B. (2018), Critical
1411   evolution of damage toward system-size failure in crystalline rock, J. Geophys. Res. 123,
1412   2017JB014964.

1413 Richter, D. and Simmons G. (1974), Thermal expansion behaviour of igneous rocks, Int. J. Rock
1414   Mech. Min. Sci. Geomech. Abstr. 15, 145–148.

1415 Roberts, N.S., Bell, A.F. and Main, I.G. (2015), Are volcanic seismic *b*-values high, and if so
1416   when? J. Volc. Geotherm. Res. 308, 127-141.

1417 Robertson, M.C., Sammis, C.G., Sahimi, M. and Martin, A.J. (1995), Fractal analysis of three-
1418   dimensional spatial distributions of earthquakes with a percolation interpretation, J.
1419   Geophys. Res. 100, 609-620.

1420 Rundle, J.B. and Klein, W. (1989), Nonclassical nucleation and growth of cohesive tensile cracks,
1421   Phys. Rev. Lett. 63, 171-174.

1422 Russ, J.C. (1994), Fractal Surfaces, Plenum Press, New York.

1423 Rydelek, P.A. and Sacks, I.S. (1989), Testing the completeness of earthquake catalogues and
1424   hypothesis of self-similarity, Nature 337, 251–253.

1425 Sammis, C.G. and Ashby, M.F., (1986), The failure of brittle porous solids under compressive
1426   stress states, Actaa Metall. 34 511-526.

1427 Sammis, C.G. and Sornette, D. (2002), Positive feedback, memory and the predictability of
1428   earthquakes, PNAS 99, 2501-2508.

1429 Sammonds, P.R., Meredith, P.G. and Main, I.G. (1992), Role of pore fluids in the generation of
1430   seismic precursors to shear fracture, Nature 359, 228-230.

1431 Schindelin, J., Arganda-Carreras, I., Frise, E., Kaynig, V., Longair, M., Pietzsch, T., Preibisch, S.,
1432   Rueden, C., Saalfeld, S., Schmid, B., Tinevez, J.Y., White, D.J., Hartenstein, V., Eliceiri,
1433   K., Tomancak, P., Cardona, A., (2012), Fiji: an open-source platform for biological-image
1434   analysis, Nature Methods 9, 676–682.

1435 Schmittbuhl, J. and Maloy, K.J. (1997), Direct observation of a self-affine crack propagation, Phys.
1436   Rev. Lett. 78, 3888-3891.

1437 Schmittbuhl, J., Schmitt, F., and Scholz, C. (1995), Scaling invariance of crack surfaces, J.
1438   Geophys. Res. 100, 5953-5973.

1439 Sethna, J.P. (2006). Statistical mechanics: entropy, order parameters, and complexity. Oxford
1440   University Press, Oxford UK.

1441 Simmons, G. and Cooper, H.W. (1978), Thermal cycling cracking in three igneous rocks, Int. J.
1442   Rock Mech. Min. Sci. Geomech. Abstr. 15, 145-148.

1443 Smith, R., Sammonds, P.R. and Kilburn, C.R.J. (2009), Fracturing of volcanic systems:
1444   experimental insights into pre-eruptive conditions, Earth Planet. Sci. Lett. 280, 211-219.

1445 Sornette, D. (2006), Critical phenomena in natural sciences: chaos, fractals, self-organization and
1446   disorder: concepts and tools, Springer, Berlin.

1447 Sornette, D. (2009), Dragon-kings, black swans and the prediction of crises, in press in the Int. J.
1448   of Terraspace Sci. and Eng. 2, 1-18, https://arxiv.org/abs/0907.4290

1449 Sornette, D. and Sammis, C.G. (1995), Complex critical exponents from renormalization group
1450   theory of earthquakes: implications for earthquake predictions, J. Phys. I [French] 5, 607-
1451   619.

1452 Stanley, H.G. (1971), Introduction to phase transitions and critical phenomena, Oxford University
1453　　　Press, Oxford UK.

1454 Sykes, L.R. and Jaumé, S. (1990), Seismic activity on neighboring faults as a long-term precursor
1455　　　to large earthquakes in the San Francisco Bay area, Nature 348, 595–599.

1456 Tapponnier, P. and Brace, W.F. (1976), Development of stress-induced microcracks in Westerly
1457　　　granite, Int. J. Rock Mech. Min. Sci. Geomech. Abstr. 13, 103-112.

1458 Thomas, A.L., & Pollard, D.D. (1993), The geometry of echelon fractures in rock: implications
1459　　　from laboratory and numerical experiments, J. Struct. Geol. 15, 323-334.

1460 Thouless (1989), Condensed matter physics in less than three dimensions, in: Davies, P. (ed.), The
1461　　　New Physics, Cambridge University Press, Cambridge UK.

1462 Turcotte, D. (1997), Fractals and chaos in geology and geophysics, Cambridge University Press,
1463　　　Cambridge UK.

1464 Tyupkin, Y.S. and Giovambattista, R.D. (2005), Correlation length as an indicator of critical point
1465　　　behavior prior to a large earthquake, Earth Planet. Sci. Lett. 230, 85–96.

1466 Utsu, T., Ogata, Y. and Matsu'ura, R.S. (1995), The centenary of the Omori formula for a decay
1467　　　law of aftershock activity, J. Phys. Earth 43, 1-33.

1468 Vasseur, J., Wadsworth, F.B., Heap, M.J., Main, I.G., Lavallée, Y. and Dingwell, D. B. (2017),
1469　　　Does an inter-flaw length control the accuracy of rupture forecasting in geological
1470　　　materials? Earth Plan. Sci. Lett. 475, 181-189.

1471 Vasseur, J., Wadsworth, F.B., Lavallée, Y., Bell, A.F., Main, I.G. and Dingwell, D. B. (2015),
1472　　　Heterogeneity: the key to failure forecasting, Sci. Rep. 5, 13259.

1473 Vinciguerra, S., Trovato, C., Meredith, P.G. and Benson P.M. (2005), Relating seismic velocities,
1474　　　thermal cracking and permeability in Mt. Etna and Iceland basalts, Int. J. Rock Mech. Min.
1475　　　Sci. 42, 900–910.

1476 Voight, B. (1988), A method for prediction of volcanic eruptions, Nature 332, 125-130.

1477 Voorn, M., Exner, U. and Rath, A. (2013), Multiscale Hessian fracture filtering for the
1478　　　enhancement and segmentation of narrow fractures in 3D image data, Comp. Geosci. 57,
1479　　　44-53.

1480 Weiss, J. (2001), Self-affinity of fracture surfaces and implications on a possible size effect on
1481　　　fracture energy, Int. J. Fract. 109, 365-381.

1482 Woessner, J. and Wiemer, S. (2005), Assessing the quality of earthquake catalogues: estimating
1483　　　the magnitude of completeness and its uncertainty, Bull. Seismol. Soc. Am. 95, 684-698.

1484 Zhang, S., Cox, S.F., and Paterson, M.S. (1994), The influence of room temperature deformation
1485　　　on porosity and permeability in calcite aggregates. J. Geophys. Res. Solid Earth, 99, 15761-
1486　　　15775.

1487 Zöller, G., Hainzl, S. and Kurths, J. (2001), Observation of growing correlation length as an
1488　　　indicator for critical point behavior prior to large earthquakes, J. Geophys. Res. 106, 2167-
1489　　　2175.